Aalto University
School of Electrical Engineering
Master's Programme in Automation and Electrical Engineering

Lassi Kääriäinen

Alternative measurement methods for impact loads of marine structures

Master's Thesis
Espoo, November 23, 2018

Supervisor:	Professor Arto Visala
Advisors:	M.Sc. (Tech.) Veikko Immonen M.Sc. (Tech.) Olli Kokko

Aalto University
School of Electrical Engineering
Master's Programme in Automation and Electrical Engineering

ABSTRACT OF
MASTER'S THESIS

Author:	Lassi Kääriäinen		
Title:	Alternative measurement methods for impact loads of marine structures		
Date:	November 23, 2018	**Pages:**	74
Major:	Control, Robotics and Autonomous Systems	**Code:**	ELEC3025
Supervisor:	Professor Arto Visala		
Advisors:	M.Sc. (Tech.) Veikko Immonen M.Sc. (Tech.) Olli Kokko		

In this thesis the prospects of different sensor technologies for impact measurements have been researched and tested. Main goal was to implement impact measurement system for an already known structure. Metallic foil strain gauges and fiber Bragg grating sensors have been previously used, but for cost reasons cheaper alternative with similar accuracy is searched for.

Researched sensors include vibrating wire strain gauges, LVDTs, accelerometers, SAW sensors, semiconductor strain gauges, photoelectric sensors and ultrasonic sensors. It was concluded that accelerometers exhibit many good qualities especially for impact measurements in difficult conditions.

A consistent method for position estimation was to detect the impact peaks from the data and only to integrate over the measured peaks to shorten the integral timespan. Minimizing the integral timespan, also minimizes the drift. To detect maximums of the impacts, clustering in conjunction with peak detection was used.

To assess the accuracy of accelerometers' position estimates, some testing with a measurement system was also made. Tests were made with capacitive, thermal and piezoelectric accelerometers with varying test parameters to see how well each type of sensor performs in different scenarios. Both the impulse duration and sensor movement range were altered according to the known system's typical ranges.

It was determined that accelerometers are a valid option for estimation of strain caused by impacts. The most accurate estimation was achieved with thermal and capacitive accelerometers. Though, piezoelectric and piezoresistive sensors should be preferred in the case of higher accelerations.

Keywords: accelerometers, impact measurements, strain gauges

Language: English

Aalto-yliopisto
Sähkötekniikan korkeakoulu
Master's Programme in Automation and Electrical Engineering

Aalto University
School of Electrical Engineering

DIPLOMITYÖN TIIVISTELMÄ

Tekijä: Lassi Kääriäinen

Työn nimi: Vaihtoehtoiset mittausmenetelmät merirakenteiden iskukuormille

Päiväys: 23. Marraskuuta 2018 **Sivumäärä:** 74

Pääaine: Control, Robotics and Autonomous Systems **Koodi:** ELEC3025

Valvoja: Professori Arto Visala

Ohjaajat: Diplomi-insinööri Veikko Immonen
Diplomi-insinööri Olli Kokko

Tässä työssä tutkittiin ja testattiin erilaisten anturien soveltuvuutta iskukuormien mittaamiseen. Työn tavoitteena on implementoida iskukuormien mittaus jo tunnetulle rakenteelle. Entuudestaan oli käytetty metallisia ja optisia venymäliuskoja, mutta kustannus-syistä johtuen etsittiin halvempaa vaihtoehtoa, jonka tarkkuus on samaa suuruusluokkaa.

Työssä vertailtiin ja tutkittiin metallilankavenymäliuskoja, LVDT-antureita, kiihtyvyysantureita, SAW-antureita, puolijohdevenymäliuskoja, välosähköisiä antureita ja ultraääniantureita. Tultiin tulokseen, että kiihtyvyysanturit soveltuvat hyvin iskukuormien mittaamiseen.

Iskukuorman aiheuttaman etäisyyden muutoksen estimoimiseen käytettiin menetelmää, jossa aluksi iskujen aiheuttamat huiput tunnistettiin datasta, jonka jälkeen vain ensimmäisen aallon yli integroitiin kahdesti paikkaestimaatin muodostamiseksi. Klusterointia käytettiin iskujen erottamiseksi toisistaan. Klusteroinnilla ja huipunhaulla saatiin integrointiväli minimoitua, jotta estimaattien arvot eivät ajelehtisi.

Anturien ja estimointimenetelmän tarkkuuden selvittämiseksi rakennettiin testijärjestelmä. Antureita poikkeutettiin erilaisilla impulssien kestoilla ja voimakkuuksilla. Testejä tehtiin kapasitiivisilla, piezosähköisillä ja termokiihtyvyysantureilla.

Kokeilla todistettiin, että kiihtyvyysanturit ovat validi vaihtoehto iskukuormien mittaamiseen. Tarkimmat estimaatit saatiin kapasitiivisella ja termokiihtyvyysanturilla. Tosin, piezosähköisten ja piezoresistiivisten kiihtyvyysantureiden käyttöä kannattaa harkita, kun kyseessä on suuret kiihtyvyydet.

Asiasanat: kiihtyvyysanturi, iskumittaus, venymäliuska

Kieli: englanti

Acknowledgements

This master's thesis is the final milestone before finishing my studies. It has also been the largest single deed of my academic journey. To make this everything possible, I wish to thank Aker Arctic for financing the work and giving me an opportunity to work on an interesting and fulfilling thesis. I especially wish to thank thesis advisors, M.Sc. Veikko Immonen and M.Sc. Olli Kokko for sharing their engineering insight and for helping me with academic writing. Furthermore, I wish to thank supervisor, professor Arto Visala for ensuring the academic and engineering requirements of this thesis have been met. I also wish to thank my family and friends for supporting me through my studies.

Espoo, November 23, 2018

Lassi Kääriäinen

Contents

Abbreviations and Acronyms

A/D conversion	Analogue to digital conversion
ASIC	Application-specific integrated circuit
CMOS	Complementary metal oxide semiconductor
DBSCAN	Density based spatial clustering of application with noise
EMI	Electromagnetic interference
FBG	Fibre Bragg grating
GF	Gauge factor; sensitivity coefficient of strain gauge
HMI	Human-machine interface
I2C	Inter-integrated circuit
IDT	Interdigital transducer
IEPE	Integrated Electronics Piezo-Electric
IIR	Infinite impulse response
LVDT	Linear variable differential transformer
MEMS	Micro electro-mechanical system
PVDF	Polyvinylidene fluoride
PZT	Lead zirconate titanite
RMSE	Root-mean-square error
SAWR	Surface acoustic wave resonator
SPI	Serial peripheral interface
TOF	Time of flight

Chapter 1

Introduction

1.1 Objective

This thesis explores different sensor technologies for a marine structure impact measurement system. Impact monitoring is needed to determine a maximum allowed workload for the optimal operation of a system. As workload is increased the health of the system is put at risk, because higher workloads result in higher stress on the structure. To know the maximum workload, the state of the structure should be measured. The primary goal of the impact monitoring system is to prevent any permanent structural damage by monitoring the stress and by adjusting the workload by the measurements.

Marine structures experience several types of loads. There are static, temperature, operational, high and low frequency dynamic loads. Static loads consist of the difference in the weight distribution on the structures. The weight is also counteracted by buoyancy that creates shear stress. Thermal loads emerge when temperature is not evenly distributed, causing uneven thermal expansion. Operational loads arise due to activities carried on the structures. [1] In this thesis the focus is put on low frequency dynamic loads that are mostly caused by crashing waves and colliding ice. The impacts also cause high frequency vibratory responses, but due to their low threat, their measurement can be ignored.

The goal of this thesis is to see, whether the monitoring system could be implemented using some other technology than metallic foil strain gauges or fiber Bragg gratings with lower cost and without compromising the accuracy of the system excessively. Currently the high costs are due to highly time consuming process of mounting and shielding the strain gauges.

Additionally, the measured structure is considered to be known, therefore other types of measurements to strain could be utilized, because the structural analysis can give the absolute maximum allowed limits for the measured quantities. For example, if laser scanner would be chosen to measure the bending of the structure, the position data contains enough information of the system to be estimate the allowed strain levels.

1.2 Requirements

First and foremost, these requirements are related to this specific implementation and are not supposed to be a general guideline for other similar works. The requirements emerge from the environment, from the sensor itself and from the measured phenomenon. The environment for the impact measurement system has set conditions that include varying temperature, moisture, vibration, potential submersion in water and minor electromagnetic interference. All these conditions can affect operation and lifespan of a sensor. Additionally, all sensors have some limitations and requirements related to their operation, which defines method of the measurements. Also the phenomenon itself that defines the whole problem, sets some parameters related to the measurements.

Varying temperature can apply loads to a sensor or affect it's operation. The sensor should be able to withstand temperature changes of tens of degrees, from approximately 0 °C to +30 °C, since that is approximately the full scale temperature range of the environment. Though, most of the heavy impacts or impacts caused by ice collisions exhibit in the lower temperatures, therefore proper operation in that temperature range is more critical.

Vibrations cause mechanical stress to sensors and can cause interference to the measurements. If the sensor contains anything fragile including sensitive electronics or mechanical parts, they might get damaged. The sensor should be able to sustain itself in the vibrating environment for long periods of time. The accelerations in the measurement environment are known to be typically within ±2 g and cause displacements of approximately ±2 mm. The vibrations consists of both low and high frequencies. Only the low end of the spectrum is needed for the position estimation, as the impacts create low frequency and high magnitude responses that contains the needed information for strain estimation.

Naturally, maritime structures are in contact with water. Therefore, the sensor should be able to operate in strongly humid conditions and possibly in submersion. Being water resistant is considered to be a benefit. Alternatively, if the previous conditions including resistance to temperature changes, physical trauma, and water are not fulfilled by the sensor alone, the sensor should be able to be protected from the conditions with relatively low effort, for example with an insulation and robust mounting.

Previously mentioned conditions might not harm the sensor in short term, but the sensor should be able to operate long periods of time. The maintenance period is 5 years for this installation, therefore that is being set as the minimum requirement for its lifespan. The whole lifespan of the installation is designed to be 25 years. So, operation of 25 years without required maintenance would be optimal.

The requirements for the dynamic properties of the measured phenomenon should be addressed. Since the purpose of the impact measurement system is to monitor stress, the system should at least be able to measure the range of loads from zero to the loads that start to cause permanent damage. For this structure permanent deformation starts to form approximately at 2000 $\mu\epsilon$. These high strains cause deformations to the structure up to 2 mm in the direction of the surface's normal. Initially, the force of an ice load collision increases rapidly, but as the ice starts to crumble the applied force starts to decay slowly. A single impact can take from tens of milliseconds to seconds. As mentioned before, the accelerations of the measured surface are within ± 2 g. The sensor should therefore be able to measure either strain up to 2000 $\mu\epsilon$ or displacements to 2 mm or another physical quantity that can be used to estimate either of these variables. The sensors should also be fast enough to measure the peaks of an impact that takes approximately 20 ms. According to Shannon-Nyquist theorem, the sampling frequency should therefore be at least 100 Hz [2]. Article of Australian defence science and technology organization states that the sampling rates should be around 100–500 Hz for marine impact loads [1].

Lastly, one of the main objectives is to decrease the costs of the monitoring system. Currently used metallic foil strain gauges are very cheap, but their installation to this difficult environment and additional required hardware including amplifiers can be expensive. To decrease the total costs, at least either the sensor with the additional hardware or the installation should be cheaper. Currently, the cost of metallic strain gauges are divided quite evenly between installation and actual hardware.

Chapter 2

Strain gauge sensors

In this chapter the technology and methods of the currently used impact load measurement system is reviewed. The system have been implemented using both resistance based metallic foil strain gauges and optical strain gauges. The metallic strain gauges have been more traditional choice, but both of the technologies are currently in use.

2.1 Resistive strain gauges

Strain gauges are made of a metallic conductor that is aligned in a mesh pattern as seen in figure 2.2. As strain is applied to the sensor, the conducting mesh is both stretched and contracted. The deformation decreases the electrical conductivity of the sensor. The change in resistance is used to sense the strain. Gauge factor, GF is a parameter that depicts the relation of applied strain and the change in resistance: [3]

$$GF = \frac{\Delta R/R}{\Delta L/L} = \frac{\Delta R/R}{\epsilon}, \tag{2.1}$$

where L and R are the nominal length of the object and nominal resistance of the strain gauge. Typical GF values for metallic strain gauges are approximately in range of 2–5. Possibly the simplest interface circuit for strain gauge measurements is a voltage divider circuit, consisting of voltage source, resistor and a strain gauge all connected in series. [4] The output voltage V_{out} of the sensor's interface circuit can be calculated with following equation:

$$V_{\text{out}} = V_{\text{in}} \frac{R_{\text{gauge}}}{R_{\text{gauge}} + R_1}, \tag{2.2}$$

where R_{gauge} is the strain gauges' current resistance altered by strain. The circuit has some weaknesses: an offset voltage exists even when the gauge is not being stressed. For example, if the resistor's resistance is same as the nominal value of the strain gauge, the output of the circuit with zero strain is half of the voltage source potential V_{in}. Also sensitivity of the output could be higher with more advanced methods. For these reasons a more complex circuit called wheatstone bridge is commonly used to improve the previous properties. In a wheatstone bridge, an additional voltage divider circuit is added in parallel. A wheatstone bridge can be seen in figure 2.1. [4]

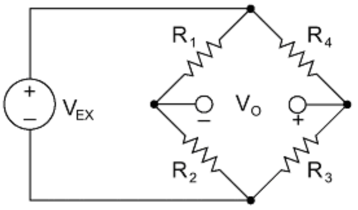

Figure 2.1: Wheatstone bridge circuit [3]

There are three configurations of the circuit that are used: quarter bridge, half bridge and full bridge, which have one, two and four strain gauges respectively. The output voltage of the wheatstone bridge is the difference of the two terminal voltages: [4]

$$V_{\text{o}} = V_+ - V_- = V_{\text{EX}}(\frac{R_2}{R_1 + R_2} - \frac{R_3}{R_3 + R_4}) \tag{2.3}$$

All of the configurations offer the same benefit of removing the offset voltage: if all the resistor values are the same then the output voltage is zero, as the coefficient for V_{EX} turns to zero. In half bridge configuration, higher sensitivity is achieved in comparison with to the quarter bridge and the voltage divider circuit due to one terminal's voltage dropping and the other's increasing, as strain is increased. Typically R_1 and R_4, or R_2 and R_3 are replaced with strain gauges, so that one of the strain gauge is stretched and the other is constricted by the strain. This is achieved by placing the gauges on different sides of the strained specimen. Other method is to replace R_2 and R_4, or R_1 and R_3 with codirectionally strained strain gauges.

In the full bridge configuration four strain gauges are used, so that the adversely placed gauges undergo codirectional strain. The full bridge configuration will further increase sensitivity of the circuit compared to half bridge configuration. [4]

Previously mentioned circuits work well as long as the temperature does not change significantly. Difference between strain gauge's and the measured

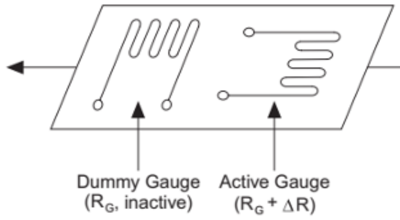

Figure 2.2: Dummy gauge installation [3]

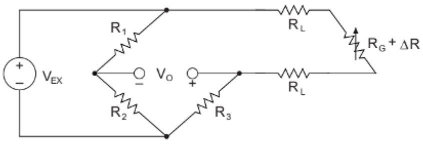

a) Two-Wire Connection

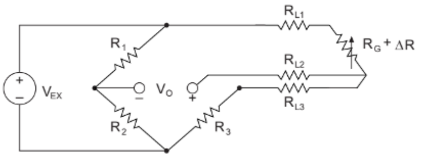

b) Three-Wire Connection

Figure 2.3: Three wire circuit [3]

specimen's thermal expansions add error in the measurements. This error can be reduced by using either strain gauges with same thermal expansion coefficient as the target material or by using half bridge, or quarter bridge with dummy strain gauges instead of the resistors. The so called dummy gauges are placed transversely to the experienced strain (figure 2.2), so that only the heat expansion increases or decreases their resistances. The dummy gauges also have to be on the same side of the specimen as the compensated strain gauge for the compensation to be inversely proportional to the strain caused by thermal expansion. [3] Naturally full bridge does not need the dummy gauges for compensation, as the bridge is already full.

Previously, the lead wire resistances have been ignored. In reality, the copper wires connected to the sensors have resistance that induces significant error to the measurements. For example, in case of using over 10 m wires the error from lead wires can be up to multiple microstrains. This problem is further escalated as the temperature changes. However, the lead wire error can be compensated using the three wire measurement method. The three wire method for quarter wheatstone bridge can be seen in figure 2.3 b. The three wire configuration adds a wire that moves the connection of positive output terminal and resistor R_3 further away towards the measured specimen and the strain gauge. Therefore a lead resistance (R_{L1} and R_2) is on the both sides of the voltage divider, and they are compensated by each other. Current of positive terminal is insignificant, therefore lead resistance R_{L2} negligible. [3]

The source voltage V_{EX} can fluctuate during measurements, which affects directly the output of the wheatstone bridge. For this reason, also the source voltage can be measured for compensation. Another method for removing DC offset is to use AC signal excitation for the wheatstone bridge [5]. DC voltage in a AC signals is easy to notice, because the DC component shifts the whole AC signal.

2.2 Optical strain gauges

Fibre Bragg grating sensors, also known as optical strain gauges, are strain or temperature sensors based on reflection of broadband light caused by Bragg gratings. In figure 2.4 the effect of Bragg gratings on broadband light can be seen. The Bragg gratings are used to reflect the light propagating in the innermost core of the optical fibre, but only certain part of the band is reflected by the grating sensor. The gratings consist of thousands of fringes that each can reflect a very low band of approximately 0.001–0.1 percentage of the band. The transmitted light is either lost or, in case of daisy chaining sensors, used again further in the fibre to interrogate more gratings. To have multiple sensors on a single optical fibre, two methods can be utilized: either multiplexing by time division or multiplexing by wavelength. The first method uses light's time of flight to determine the location of the sensor. The other method uses wavelength separated sensors. [6]

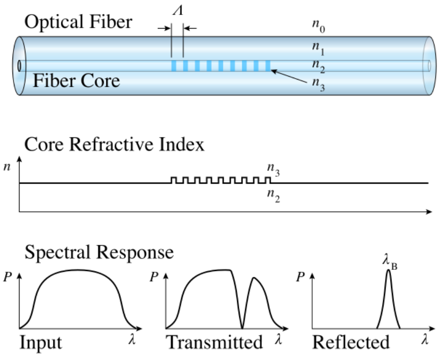

Figure 2.4: Bragg gratings[7]

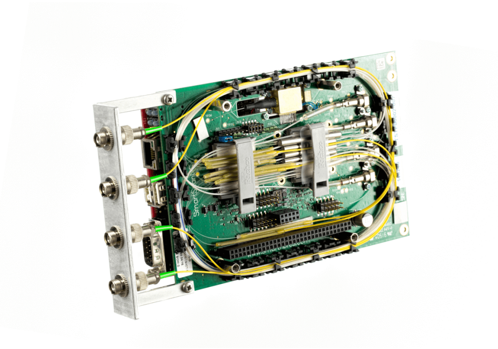

Figure 2.5: Interrogator [8]

In order to determine the axial strain, special hardware is needed. The interrogator is a device that both casts the broadband light and does the required signal processing for the reflection. The signal processing typically includes measurements of the light intensity in function of wavelength and the detection of individual sensors based on their response times or wavelengths. A commercial interrogator unit without it's cover is presented in figure 2.5. Usually the interrogators have multiple channels, as seen in the picture to increase the amount sensors to be able to be connected simultaneously. In case of using only single FBG sensor at a time, a spectrometer in conjunction with a broadband light source would be sufficient. [9]

The strain and temperature can be deduced from each sensors' shifted centre wavelength of peak intensity. Bragg condition is used to calculate the centre wavelength of the reflected light band: [10]

$$\lambda_0 = 2n_{\text{eff}}\Lambda \tag{2.4}$$

The response, the change in the reflected band of the sensor is affected by two conditions. First, the change in the refraction index, n_{eff} in the light propagating innermost core of the optical fibre. Second, the change of pitch length of Bragg gratings, Λ [10]. Equation

$$\frac{\Delta\lambda}{\lambda_0} = (1 - \frac{n_{\text{eff}}^2}{2}p_{12})\epsilon_1 - \frac{n_{\text{eff}}^2}{2}(p_{11}\epsilon_2 + p_{11}\epsilon_3) + \beta_0\Delta T \tag{2.5}$$

describes the change in the refracted band, where ϵ_1 is the axial strain, ϵ_2 and ϵ_3 are the principal strains in the optical strain gauge. Coefficients p_{11} and p_{12} are the photoelastic coefficients. The values vary slightly depending on the materials used in the fibre core. β is a combination of thermo-optic coefficient and thermal expansivity. The principal strains only constitute approximately 2 percent of the total wavelength variation. Therefore, for practical purposes, following simplified form can be used:

$$\frac{\Delta\lambda}{\lambda_0} = GF\epsilon_1 + \beta\Delta T \tag{2.6}$$

$$\beta = \beta_0 + GF(\alpha_2 - \alpha_1). \tag{2.7}$$

GF is strain gauge factor describing the relation of strain and shifted centre wavelength. The second equation can be used for additional thermal compensation. Two thermal expansivity coefficients α_2 and α_1 are introduced for the optical fibre and for the host material respectively. [10]

The benefits of FBG sensors are many compared to the traditionally used strain gauges. First, since the signals of FBG sensors are based on electromagnetic radiation, instead of electronic signals, the sensors are practically immune to electromagnetic interference. Therefore, they can be positioned near high voltage devices or other hazardous areas. The sensors can be also positioned much further than electrical sensors since the data is propagated in optical fibre instead of copper wire. The sensors can actually be up to >50 km away from the interrogator. In addition one optical fibre channel can contain typically up to >20 sensors, or with some interrogation techniques >100 sensors. This will decrease the amount of wiring is needed for the system. Since the measurements are based on the wavelengths, the measurements are independent from the intensity of the light source. Slight long term variation in the intensity will not affect the measurements. In resistive strain gauge technology the input voltage to the strain gauge will directly affect it's output, if it is not compensated. Therefore FBGs offer better long term stability. [6]

2.3 Positioning of strain gauges

Previously we have been measuring only one directional extensional strains. In some application it is known in which direction does the highest normal strains or principal strains are applied. In those cases the most logical sensor mounting method is to point the sensors to measure the highest strain. But if the directions are not known or the direction of principal strains change during the measurements, how to align the sensors to the specimen's surface? The state of the surface's strain can be modelled either as principal strains and their directions or as x and y components of strain combined with it's shear strain. To solve these parameters two-dimensional stress transformation equations can be used:

$$\epsilon_{\mathrm{x'}} = \epsilon_{\mathrm{x}}\mathrm{cos}^2\theta + \epsilon_{\mathrm{y}}\mathrm{sin}^2\theta + \gamma_{\mathrm{xy}}\mathrm{sin}\theta\mathrm{cos}\theta \tag{2.8}$$

$$\epsilon_{\mathrm{y'}} = \epsilon_{\mathrm{x}}\mathrm{sin}^2\theta + \epsilon_{\mathrm{y}}\mathrm{cos}^2\theta + \gamma_{\mathrm{xy}}\mathrm{sin}\theta\mathrm{cos}\theta \tag{2.9}$$

$$\gamma_{\mathrm{x'y'}} = 2(\epsilon_{\mathrm{y}} - \epsilon_{\mathrm{x}})\mathrm{sin}\theta\mathrm{cos}\theta + \gamma_{\mathrm{xy}}(\mathrm{cos}^2\theta - \mathrm{sin}^2\theta) \tag{2.10}$$

Where: $\epsilon_{\mathrm{x}}, \epsilon_{\mathrm{y}}, \gamma_{\mathrm{xy}}$ are the x- and y-components of extensional strains and the shear strain. θ is defined as the counter-clockwise rotation from x axis to x' axis. The previous equations can also be expressed in the double angle form: [11]

$$\epsilon_{\mathrm{x'}} = \frac{1}{2}(\epsilon_{\mathrm{x}} + \epsilon_{\mathrm{y}}) + \frac{1}{2}(\epsilon_{\mathrm{x}} - \epsilon_{\mathrm{y}})\mathrm{cos}2\theta + \frac{\gamma_{\mathrm{xy}}}{2}\mathrm{sin}2\theta \tag{2.11}$$

$$\epsilon_{\mathrm{y'}} = \frac{1}{2}(\epsilon_{\mathrm{x}} + \epsilon_{\mathrm{y}}) - \frac{1}{2}(\epsilon_{\mathrm{x}} - \epsilon_{\mathrm{y}})\mathrm{cos}2\theta - \frac{\gamma_{\mathrm{xy}}}{2}\mathrm{sin}2\theta \tag{2.12}$$

$$\gamma_{\mathrm{x'y'}} = -(\epsilon_{\mathrm{x}} - \epsilon_{\mathrm{y}})\mathrm{sin}2\theta + \gamma_{\mathrm{xy}}\mathrm{cos}2\theta \tag{2.13}$$

Common solution is to have three strain gauges in so called rosette formation. In theory, having three measurements from a single point would yield

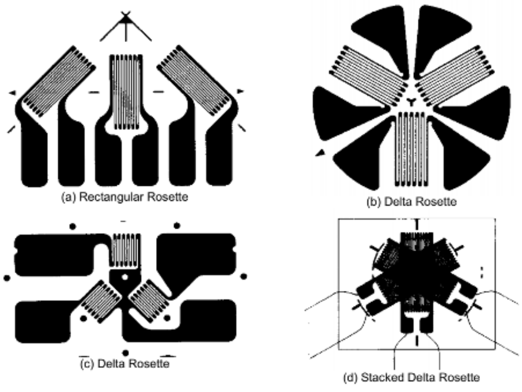
(a) Rectangular Rosette

(b) Delta Rosette

(c) Delta Rosette

(d) Stacked Delta Rosette

Figure 2.6: Strain gauges in rosette [12]

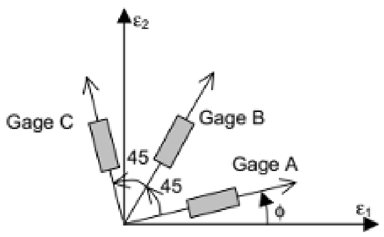

Figure 2.7: Angle of principal strain coordinate system [12]

the best representation of the point's strains. But, in reality stacking three strain gauges (Figure 2.6, d) together is often prone to failures of installation. Therefore, usually having the sensors separately installed achieves better results. Figure 2.6 a-c shows rosette strain gauge installation formations. [12]

To calculate the principal strains from a rectangular rosette formation, we can use the two-dimensional stress transformation equations. Let's choose ϕ to be the angle of the principal strain coordinate system in relation to the rosette x and y-coordinate system. Additionally, let us choose $\epsilon_{\mathrm{A}}, \epsilon_{\mathrm{B}}, \epsilon_{\mathrm{C}}$ to be the extensional strains measured by the three strain gauges, and ϵ_1, ϵ_2 to be the principal strains. In the rectangular rosette configuration each strain gauge is rotated by 45° in respect to the neighbour gauges. Therefore the strains can be expressed using equations 2.14, 2.15 and 2.16 [12]

$$\epsilon_{\mathrm{A}} = \frac{\epsilon_1 + \epsilon_2}{2} + \frac{\epsilon_1 - \epsilon_2}{2}\mathrm{cos}2\phi \tag{2.14}$$

$$\epsilon_{\mathrm{B}} = \frac{\epsilon_1 + \epsilon_2}{2} + \frac{\epsilon_1 - \epsilon_2}{2}\mathrm{cos}2(\phi + 45^\circ) \tag{2.15}$$

$$\epsilon_{\mathrm{C}} = \frac{\epsilon_1 + \epsilon_2}{2} + \frac{\epsilon_1 - \epsilon_2}{2}cos2(\phi + 90^\circ) \tag{2.16}$$

Note that as the strain state is expressed using principal strains the shear strain becomes zero [11]. Now we have three equations and three unknown parameters to solve. Solving the linear equations yields following results: [12]

$$\epsilon_{1,2} = \frac{\epsilon_{\mathrm{A}} + \epsilon_{\mathrm{C}}}{2} \pm \frac{1}{\sqrt{2}}\sqrt{(\epsilon_{\mathrm{A}} - \epsilon_{\mathrm{B}})^2 + (\epsilon_{\mathrm{B}} - \epsilon_{\mathrm{C}})^2} \tag{2.17}$$

$$\phi = \frac{1}{2}\tan^{-1}(\frac{\epsilon_{\mathrm{A}} - 2\epsilon_{\mathrm{B}} + \epsilon_{\mathrm{C}}}{\epsilon_{\mathrm{A}} - \epsilon_{\mathrm{C}}}) \tag{2.18}$$

Also, the three equations can be formed for the delta rosette form by using the two-dimensional shear transformation equation and by separating the angles by 120° instead of the previously used 45° and by setting the shear strain to zero. It can be solved that the solution of delta rosette principal strains and their direction is following: [12]

$$\epsilon_{1,2} = \frac{\epsilon_{\mathrm{A}} + \epsilon_{\mathrm{B}} + \epsilon_{\mathrm{C}}}{3} \pm \frac{\sqrt{2}}{3}\sqrt{(\epsilon_{\mathrm{A}} - \epsilon_{\mathrm{B}})^2 + (\epsilon_{\mathrm{B}} - \epsilon_{\mathrm{C}})^2 + (\epsilon_{\mathrm{C}} - \epsilon_{\mathrm{A}})^2} \tag{2.19}$$

$$\phi = \frac{1}{2}\tan^{-1}(\frac{\sqrt{3}(\epsilon_{\mathrm{C}} - \epsilon_{\mathrm{B}})}{2\epsilon_{\mathrm{A}} - \epsilon_{\mathrm{B}} - \epsilon_{\mathrm{C}}}) \tag{2.20}$$

Chapter 3

Overview of alternative sensors

In this chapter, possible technologies for alternative impact load measurement system are researched. For each sensor their operating principle and typical properties are reviewed. Their suitability for impact measurements is later assessed in the next chapter. Sensors have been chosen based on how well they seem to fulfil the requirements in the introduction. Technologies that have before been used in structure health monitoring applications such as in bridges and air planes have been favoured in the selection. This is due to the fact that those sensors have previously been proved to be able to solve difficult measurement problems.

3.1 Vibrating wire strain gauge

Vibrating wire strain gauges, also known as acoustic strain gauges, are strain sensors consisting of a tensioned and firmly attached wire. As the wire is strained or loosened the natural frequency is changed. The wire is set to vibrate by a plucking coil that is part of the sensor. A pickup coil is used to read the frequency of the vibration. Though, some variations of the sensor only contain a single coil. In that case the measurement should be done immediately as the vibration starts to dampen as the excitation has ended. In figure 3.1 can be seen a cross-section of a vibrating wire sensor. [13]

The sensor is well suited for long term monitoring, because the strain is derived from the resonant frequency. And the frequency of an electrical signal containing the strain information is imperturbable. For example, frequency measurements are not prone to errors caused by fluctuating voltage levels. Additionally, the need for amplification is less for frequency measurements than for voltage measurements. There has even been an experiment to prove the point by comparing measurements of a sensor without a signal amplifier

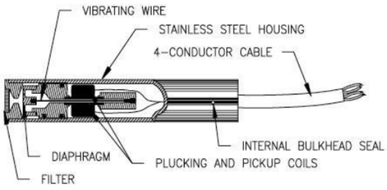

Figure 3.1: Vibrating wire sensor structure [13]

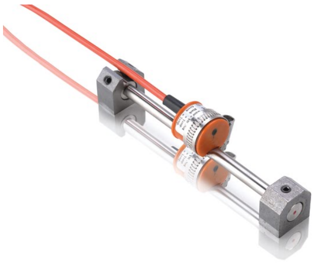

Figure 3.2: Vibrating wire sensor [14]

and with cable lengths of 1.5 m and 2.7 km. The readings were within 0.1%. Though, electro-magnetic interference shielding wires were used. [15] The strain can be derived from the following equation:

$$\epsilon = \frac{4L^2\rho}{E}(f_1^2 - f_2^2) = GF(f_1^2 - f_2^2), \tag{3.1}$$

Where L is the length of the vibrating wire, ρ is the density of the wire and E is Young's modulus of the wire's material. Variables f_1 and f_2 are initial and changed natural frequencies respectively. The equations can also be abstracted using the gage factor that can be either found by theoretical means or by measuring. [15]

Generally two different types of vibrating wire sensors exist. The first type is a surface mountable sensor. They are usually either glued, welded or bolted to the measured specimen. A weldable surface mount vibrating wire sensor can be seen in figure 3.2. The second type, embedded vibrating wire sensors are inserted inside of structures as they are being built. For example, they could be inserted in a mould of a concrete structure before the concrete has been cast. In this case, a good mounting point could be located between two reinforcing steel bars inside the concrete. [16]

Similarly to the optical and resistive strain gauges, vibrating wire are susceptible to errors caused by differences in thermal expansions of the sensor and the host material. The strain caused by thermal expansion can be calculated by following equation:

$$\epsilon_{\mathrm{T}} = (\alpha_{\mathrm{W}} - \alpha_{\mathrm{S}})\Delta T, \tag{3.2}$$

Where $\alpha_{\mathrm{W}}, \alpha_{\mathrm{S}}$ are the thermal expansion coefficients and ΔT the difference in the temperature. To get the strain from mechanical stress thermal strain can be subtracted from the measured strain.[16]

There are different methods for the excitation of the sensor. The simplest of them is impulse excitation consisting of a single high voltage pulse. Another method is to have AC current to excite the sensor. Different waveforms and range of frequency of sweeping should be considered. The benefit of impulse excitation is that measurements can be done more quickly than in the frequency sweeping method. Though, the simplicity of implementation comes with some disadvantages. The impulse excitation has lower dampening time and amplitude than the AC signal excitation. The impulse method also requires higher excitation voltage to be used than frequency sweeping, which could decrease the sensors lifespan. In the continuous frequency sweeping, square waves yield higher output amplitude than sinusoidal excitation signals, thus increasing also the dampening times. In practise, selection of excitation signal depends also on the available hardware. [13]

3.2 Linear Variable Differential Transformer

A linear variable differential transformer (LVDT, figure 3.3) is a sensor for measuring distance. The sensor consists of a transformer and a moveable magnetic core. To measure position or strain, the housing of the transformer and the rod are used as the mounting points. As the specimen moves, the rod inside of the transformer moves and affects the induced voltage. The transformer consists of a primary coil and two secondary coils. The primary coil is connected to an excitation AC voltage source that induces voltage to the secondary coils. Difference in a reading results from the displacement of the ferromagnetic rod. As the rod is moved, the voltage of one of the secondary coils is increased and the voltage on the other coil is decreased linearly. Linearity on the sensor's designed dimension of movement is good (approximately within 0.5%), but the mismatch of the secondary windings and leakage inductance are sources of error. [17]

The output of the sensor is the difference of the two secondary coil voltages. Note that the voltages are in AC, therefore the voltage of signals' subtraction does not bear the information of direction of the magnetic core's displacement. [17] For this reason, usually the sensor has also a signal conditioning circuit that first rectifies the voltages. In figure 3.4 is presented a functional schematic of AD598 LVDT signal conditioner. In addtion to rectifier the AD598 signal conditioner has amplifiers and filters to increase robustness.

LVDTs offer many good qualities. LVDTs have high resolution and linearity. Stroke length of the cylinder can be manufactured to a length of choosing. And since the sensors are not in contact with the measured specimen they

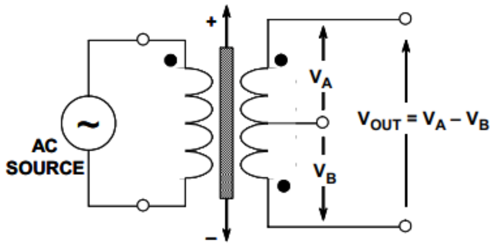

Figure 3.3: LVDT sensor [17]

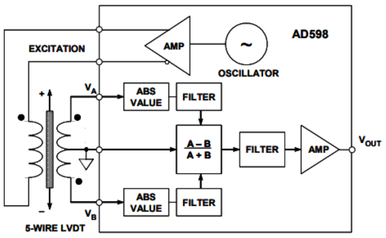

Figure 3.4: LVDT sensor signal conditioning circuit [17]

can be easily shielded. For this reason LVDTs are often selected for applications where environmental conditions are harsh. They have been used for example in nuclear power plants and in Cern's Large Hadron Collider. [18] The resistance to temperature is high as well. Hermetically sealed LVDTs can withstand temperature changes of hundreds of degrees. Though, the temperature also affects the sensitivity of the sensor. The majority of it is explained by the differences in the thermal expansions and the impedance changes in the electronics related to the LVDT sensor. The changes in the resistance of secondary electronics are negligible if the sensor has high impedance. Also the changes of magnetic properties of the sensor are considered negligible. [19]

3.3 Accelerometers

Accelerometers are electromechanical sensors for measuring accelerations. They can be categorized to AC response accelerometers and DC response accelerometers. AC response accelerometers are sensors with outputs coupled in AC and respond only to dynamic accelerations. They are based on piezoelectric effect. In addition to AC-response accelerometers there are DC response accelerometers that are typically based on piezoresistivity or capacitance. [20] [21]

Piezoelectric effect is a phenomenon in which physical deformation of a material causes electrical charge. This can be demonstrated, for example, with quartz that is a common piezoelectric crystal. In figure 3.5 polarization vectors P_1, P_2 and P_3 can be seen. They describe the polarity of the crystal. In unstressed state the sum of the polarization vectors is zero, which results in zero charge. But if force is applied perpendicularly with X-coordinate axis the sum of the vectors becomes non-zero, producing a charge. The crystal will also be polarized if force is applied to the Y-axis, but the polarity is on the same side as with the case of X-axis stress. [22]

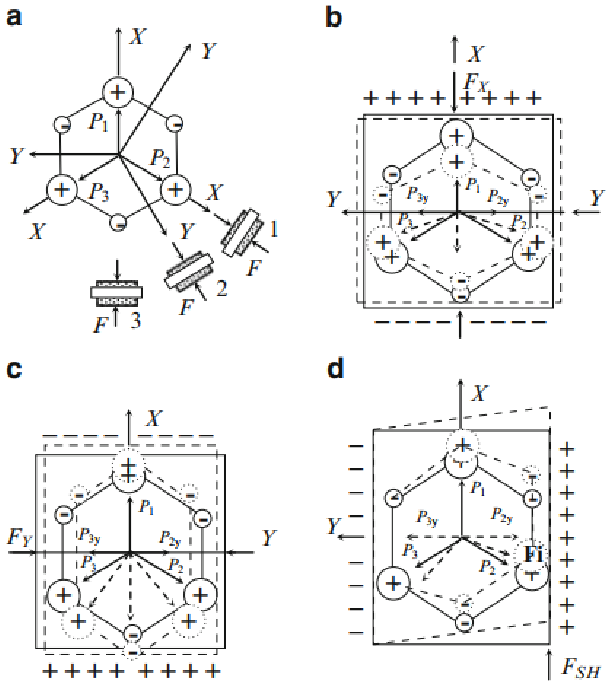

Figure 3.5: quartz crystal structure [22]

Instead of using piezoelectric crystals for sensing purposes, usually piezo polymers are used. The most common piezoelectric sensor material type is lead zirconate titanite (PZT). PZT is made by doping lead, zirconium and titanium oxides with different elements to obtain various properties. The mixture is heated and mixed with a binder to form the piezoceramic material. The material of PZT sensors has high elastic modulus, so it is capable of withstanding high strains and not to be permanently deformed. The material of PZT sensors is mechanically isotropic, but poling of tangential and normal directions of a plane are transversely isotropic. This can be seen in figures 3.6 and 3.6. The piezoelectric coefficient of directions 1 and 2 are inverse compared to direction 3. The Young's modulus of PZT is similar to aluminium, therefore it is suitable for enivironments with high forces. [23]

Another common material for piezoelectric sensors is a polymer called polyvinylidene fluoride (PVDF) that consists of long chains of $CH2_2 - CF_2$ monomers. The hydrogen atoms act as positive poles and fluorine acts as negative poles. In liquid form it is has no dipole moment, because of the free

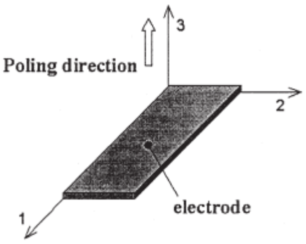

Figure 3.6: Poling directions [23]

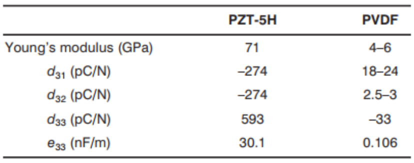

	PZT-5H	PVDF
Young's modulus (GPa)	71	4–6
d_{31} (pC/N)	–274	18–24
d_{32} (pC/N)	–274	2.5–3
d_{33} (pC/N)	593	–33
e_{33} (nF/m)	30.1	0.106

Figure 3.7: Pizoelectric sensor parameters [23]

orientation of the molecules. But after solidification the molecules are mostly aligned to the direction of the strain causing permanent dipole moment. PVDF is not mechanically nor electrically isotropic, because the material consists of long polymer chains. Therefore, the magnitude and polarity of the charge depends on the direction of the strain. PVFD has considerably lower Young's modulus, therefore it strains with lower force, but generates less charge per strain as the piezoelectric coefficient is lower. [23]

To model the piezoelectric sensor, one can model it as a charge generator and as a parallel plate capacitor. The relation of strain and voltage generated from the strain can be calculated using following equations:

$$\epsilon = \frac{V_{\mathrm{c}} C_{\mathrm{p}}}{S_{\mathrm{q}}} \tag{3.3}$$

$$C_{\mathrm{p}} = \frac{e_{33} l_{\mathrm{c}} b_{\mathrm{c}}}{t_{\mathrm{c}}} \tag{3.4}$$

$$S = d_{31} Y_{\mathrm{c}} l_{\mathrm{c}} b_{\mathrm{c}}, \tag{3.5}$$

where V_{c} is voltage, S_{q} is the sensor's sensitivity parameter and C_{p} is the capacitance of the sensor. The capacitance is defined by the $l_{\mathrm{c}}, b_{\mathrm{c}}, t_{\mathrm{c}}$, length, width and thickness of the sensor. Parameter e_{33} is the dielectric permittivity. Equation for sensor's sensitivity, S_{q} presents new parameters for the piezoelectric coefficient for normal strain and Young's modulus of the sensor material, d_{31}, Y_{c} respectively. [23]

Now that the relationship between measured voltage and the strain is known, a method for the voltage measurement is introduced. The piezoelectric sensors have very high output impedance, which makes the measurement device's comparable impedance affect the voltage reading. To tackle this problem, charge amplifier circuit is presented. The circuit can be seen in figure 3.8. The circuit lowers the output impedance to megaohm range

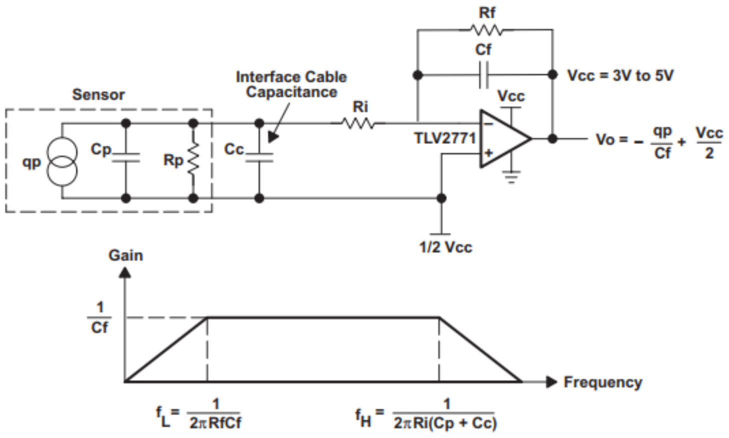

Figure 3.8: Charge amplifier circuit [24]

while giving the system additional protection against over voltage. The basic working principle is to have a voltage follower circuit using a operational amplifier. The sensor charges C_f and the negative terminal of the amplifier. Resistor R_f bleeds slowly the charge away to avoid saturation of the amplifier. Positive terminal of the amplifier is used to give the output voltage a positive bias. The output is half of V_cc when there is zero strain. Note that the circuit works as a high-pass filter, therefore components $R_\mathrm{f}, R_\mathrm{c}$ should be chosen so that the cut-off frequency is suitable for the phenomenon being measured. [24] There exists two main types of AC response accelerometers: charge mode piezoelectric and voltage mode piezoelectric. The difference is that charge mode amplifier does not have a charge amplifier embedded into the sensor. The benefit is that the dynamic range can be configured remotely, as the amplifier parameters are able to be configured. Also the sensor itself is more durable, as the fragile circuitry is at safe position, out of the harsh environment. The IEPE (Integrated Electronics Piezo-Electric) labeled voltage mode piezoelectric accelerometers advantage is they do not need special low-triboelectric noise shielded cable, for example in coaxial cable configuration. Because the amplifier is before the cables, then the effect of capacitance of the cables is negligible, therefore it does not affect the charge amplifier. [20]

Compared to to AC-response accelerometers, DC-response accelerometers are coupled with DC outputs and can also measure static accelerations. There exists multiple implementations of DC-response accelerometers. Two main types are capacitive and piezoresistive. DC-response accelerometers often utilize MEMS (Micro electro-mechanical system) technology, due to compact size and low cost. [20] MEMS systems have structures smaller than 100 μm and are manufactured using micro-fabrication methods instead of typical machining methods. MEMS systems are usually fabricated from silicon, polymer, glass, quartz or metal materials.

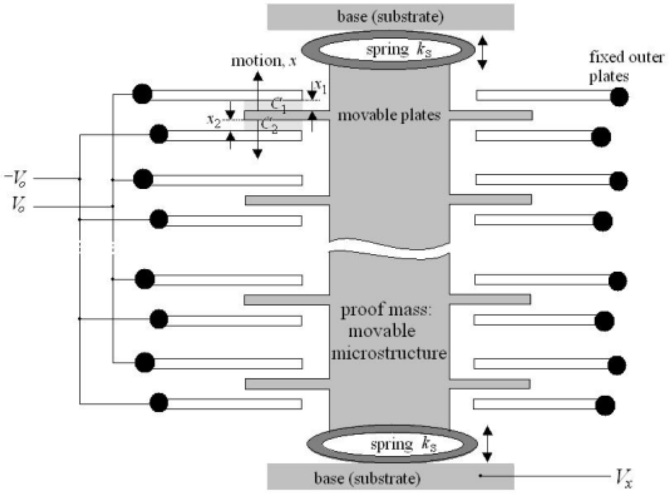

Figure 3.9: Capacitive MEMS accelerometer [25]

Capacitance based accelerometers consists of a spring mounted parallel plate capacitor microstructure. An example of variable capacitance MEMS microstructure can be seen in figure 3.9. As force is applied to the accelerometer, pendulum like structure called proof mass is moved off center. This causes the distance between the parallel plates to change, thus changing capacitance of two capacitors, C_1, C_2. The change of capacitances is then transferred to change in the output.[25]

The capacitance of the parallel plate capacitors are following:

$$C_0 = \frac{\epsilon_0 \epsilon A}{d} = \frac{\epsilon_{\mathrm{A}}}{d} \tag{3.6}$$

$$C_1 = \frac{\epsilon_{\mathrm{A}}}{d + x} = C_0 - \Delta C \tag{3.7}$$

$$C_2 = \frac{\epsilon_{\mathrm{A}}}{d - x} = C_0 + \Delta C, \tag{3.8}$$

where ϵ is permittivity of the material between electrodes, A is the area of the electrodes and d is the distance between them. x is the displacement of the proof mass caused by acceleration. The output of the proof mass system is modulated square wave AC signal, whose amplitude is [25]

$$V_{\mathrm{x}} = V_0 \frac{C_2 - C_1}{C_2 + C_1}. \tag{3.9}$$

The voltage V_{x} is then amplified and demodulated to form the sensor output. [25] The benefit of capacitance based MEMS sensors is that they have extremely high stability in altering temperatures. They have low band of frequency responses (0-1 kHz), but high sensitivity compared to the other types. Sensitivity of 1 V/g is not uncommon. The capacitance accelerometers also exhibit phenomenon called "DC responding", meaning that they output response of 1 g, when they are positioned coaxially with gravity. This property is useful in measuring vertical accelerations for example in elevators. [26] The disadvantage of capacitance based accelerometer is that they often suffer from poor signal to noise ratio.[20]

Piezoresistivity is a phenomenon that increases material's resistivity as the material is under stress. Piezoresistive accelerometers consist of one-dimensional cantilever and proof mass system. As the system is in acceleration, cantilever is strained and piezoresistor mounted on the cantilever has it's resistance changed according to the strain. Typical implementation of reading the state of the piezoresistive sensor is to use wheatstone bridge. [27] Wheatstone bridges have already been discussed in chapter 2.1. Additionally, most modern piezoresistive accelerometers have embedded ASICs (Application-specific integrated circuit) for signal conditioning, since the readings are temperature dependant.[20] In piezoresistive accelerometers there are pn-junctions, whose conductivity is increased by temperature. The phenomenon is explained by higher number of charge carriers or electron-hole pairs in the semiconductor. The scale of change in the sensitivity is ±10% on the whole temperature range. Piezoresistive accelerometers have low sensitivity, therefore they work best for high impact shock measurements. They can handle accelerations of thousands of g's and have excellent signal to noise ratio. Typical application is for example transportation crash sensing. [26] [20]

Additionally, there are so called thermal accelerometers. Thermal accelerometers consist of a pair of temperature sensors, for example thermocouples and a resistive heater placed in an air cavity (Figure 3.11). The heater is positioned between the two temperature sensors heating the air in a cavity. When there is no acceleration, the heat is distributed symmetrically in the cavity. As the accelerometer is accelerated, the less dense heated air is moved in the direction of the acceleration and the more dense cool air is moved in the opposite direction. Now the heat is distributed unevenly and the temperature sensors have different readings that are linearly dependent on the acceleration and its direction.[21]

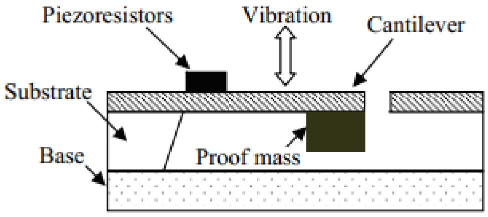

Figure 3.10: Piezo-resistive MEMS accelerometer [28]

The benefits of thermal accelerometers are good resistance to high accelerations up to 10 000 g's and generally low failure rate. This property is due to the robust sensor design having no moving parts. Also by not having cantilever/spring system, the sensor has no resonance error or in other words error caused by excitation that is close to the sensors resonant frequency. The negatives of the sensor are higher current consumption compared to the previous accelerometer technologies and smaller bandwidth. The bandwidth of thermal sensors reach typically to around 30 Hz and with added signal processing circuits up to 100 Hz. [21]

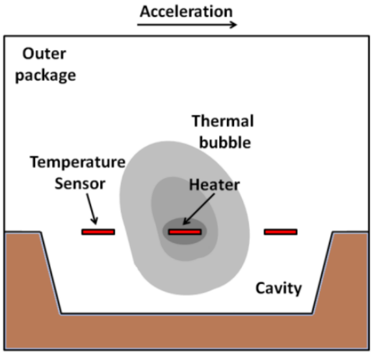

Figure 3.11: Thermal accelerometer operating principle [29]

3.4 Surface acoustic wave resonator sensors

SAW or SAWR (Surface acoustic wave resonator) technology has been typically used in signal processing applications. But recently effort has been put to investigate the possibility of using SAW for sensing applications. There are high expectations due to their compact size, wirelessness, passivity and high accuracy. They have already been used in various harsh conditions including automotive application, inside jet engines and aircraft wing structures.[30]

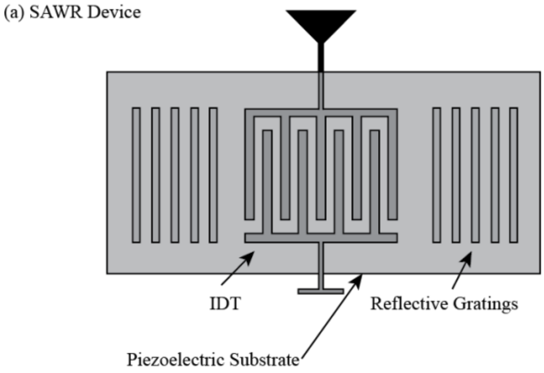

Figure 3.12: SAW sensor structure [30]

SAW sensors consist of a piezoelectric polished plate. Two reflective gratings and an IDT (Interdigital transducer) have been manufactured on the plate. The IDT element acts as an electrode pair generating and detecting the SAW waves. Transduction of electricity to mechanical waves is can be achieved with piezoelectric materials. The purpose of the gratings is to reflect and contain the waves. The IDT element is connected to a RF antenna transmitting the waves. The response of the sensor is maximized when the sensor is excited by a RF signal of following frequency:[30]

$$f_\mathrm{c} = v_\mathrm{s}/2p, \tag{3.10}$$

where v_s is the surface wave velocity and p is the pitch of the IDT element. The pitch of the sensor is affected by the mechanical structure of the sensor. As the sensor is strained the frequency f_c is modulated accordingly.

The interrogation of the sensor is done with RF wave pulses with a remote interrogator. The sensor sends pulses with decaying frequencies. The highest magnitude response and it's corresponding excitation RF pulse holds the information of the sensor's strain. [30]

3.5 Semiconductor strain gauges

Like traditional metallic strain gauges, the semiconductor strain gauges are based on the effect of change in resistance due to strain applied to the sensor.

But in addition to the deformation of the conducting material, majority of the resistance change is explained by piezoresistive effect. In figure 3.13 can be seen a foil type semiconductor strain gauge.

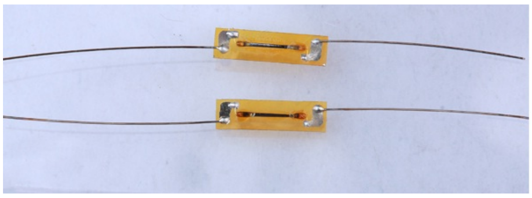

Figure 3.13: Semiconductor strain gauge [31]

Piezoresistivity is present in all materials to some degree, but in silicon semiconductors it is considerably higher. The resistivity of a semiconductor can be expressed by it's number of charge carriers N_i and their average movement μ_{ave}: [32]

$$\rho = \frac{1}{eN_i\mu_{\text{ave}}} \tag{3.11}$$

Where e is the electronic charge. The magnitude and sign of the charge depends on the type of semiconductor. The applied strain affects the number of charge carriers and their average movement. For single axial strain with coaxial current, the change in resistivity $\Delta\rho/\rho_0$ can be expressed with following equation:[32]

$$\frac{\Delta\rho}{\rho_0} = \Pi_{\text{L}}\epsilon Y, \tag{3.12}$$

where Π_{L} is longitudinal piezoresistive coefficient, ϵ is strain and Y is Young's modulus for the semiconductor. Typically Young's modulus for silicon between 130–188 GPa [33]. The gauge factor can be defined the same as in the case of metallic strain gauges, but it can also be defined using the piezoresistive coefficient:[32]

$$GF = \frac{\Delta R}{R_0\epsilon} = 1 + 2v + \Pi_{\text{L}}Y, \tag{3.13}$$

where v is Poisson's ratio. The first two terms describe the change in the resistance due to mechanical deformation and the third term is the sensitivity caused by the piezoresistivity.[32]

The benefits of semiconductor strain gauges is their superior sensitivity compared to metallic strain gauges. Gauge factor of a metallic strain gauge is typically 2-5 and in semiconductor gauges gauge factors typically reach values over 100.[34] Additionally, the piezoresistive area in the sensor can be very small, approximately 10 nm^2. Therefore, the sensors can be built to be smaller than many other strain sensors including metallic strain gauges.

Temperature expansion of semiconductor strain gauges is negligibly small, but temperature dependence of resistance is high. Choosing similar thermal expansion as the host material is therefore impractical, therefore the compensation should be done either in software or by electronics. Compensation using electronics is presented in chapter 2.1. Young's modulus of semiconductor strain gauges is considerably high. The host material should be stiff for its straining not to be constrained by the sensor. [35]

3.6 Photoelectric sensors

Photoelectric sensors, also known as diffuse reflection sensors, are based on electromagnetic radiation, usually laser or LED technology. There are two robust methods for distance measurements: TOF (Time of flight) and triangulation. Both methods are based on the reflection of the transmitted light.

In triangulation, the angle of reflected light is measured. The geometry of the reflected light can be seen in figure 3.14. The laser emits a point beam that is reflected from the object to the camera. The distance from the sensor to the object, q can be calculated by following formula: [36]

$$q = \frac{fs}{x} \tag{3.14}$$

The relation of distance between the sensor and object and the distance between the laser and the object is following: [36]

$$q = \sin(\beta)d \tag{3.15}$$

Using aforementioned equations shows the non-linear relation of image's pixel location, x and the distance of object q: [36]

$$\frac{dq}{dx} = -\frac{q^2}{fs} \tag{3.16}$$

The sensitivity of the triangulation sensor, dq/dx is quadratically proportional to the distance of the object, q. This quadratic relation induces design problems for the sensor on long measurement distances. Another problematic property of the triangulation method is that there is an area in close vicinity of the sensor that can not be measured. If the object is too close to the sensor the light can not reflect to the camera. [36]

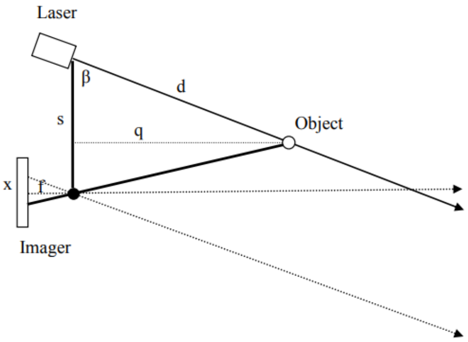

Figure 3.14: Triangulation [36]

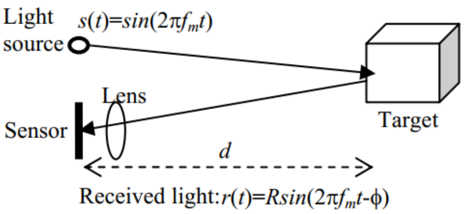

Figure 3.15: Time of flight [37]

The alternative for triangulation is TOF method. Typically the system consists of a light source and light sensor, for example a CMOS (Complementary metal oxide semiconductor) sensor. The transmitted light is modulated by switching it on and off with a certain frequency. As the light is reflected from the object, the phase of the light is measured. Based on the phase shift and known speed of light the distance travelled can be deduced. [37]

The distance travelled by the light is following:

$$d = \frac{c\phi}{4\pi f_{\mathrm{m}}}, \tag{3.17}$$

where c is the speed of light, ϕ is phase shift and f_{m} is the modulation frequency of the transmitted light. Frankly, the maximum phase shift that can be detected is a full cycle of a modulation period. This would limit the measured distance to $c/2f_m$ as phase shifts over one period would be undistinguishable form the phase shifts valued less than one full period. For example with modulation frequency of 50 MHz the maximum range corresponding to a full period's phase shift would be only 3 m. However, most modern time of flight distance sensors have advanced signal processing circuits to further increase the range. [37]

The benefits of photoelectric sensors are that they have high range, are non-contact sensors and have good resistance to electro-magnetic interference. Non-contact sensors offer capability of measuring locations that are hard to reach. Light or electromagnetic radiation in general is not strongly affected by electromagnetic interference, though the electronics related to the sensor are. The most important source of noise and error for these type of sensors are particles and moisture in air. Abnormalities in the air reflects light unpredictably, thus creating errors in the measurements. Also external light sources, especially infra-red can interfere with transmitted signals or give false readings. [38]

3.7 Ultrasonic sensors

Like the photoelectric sensors, ultrasonic sensors are non-contact distance sensors. But instead of using light, ultrasonic sound pulses are used to determine distances. Ultrasonic sensors are often based on a time of flight method called pulse-echo method. There are also measurement methods using the amplitude of echo, but they suffer from low resolution. A schematic of the pulse-echo method can be seen in figure 3.16. [39]

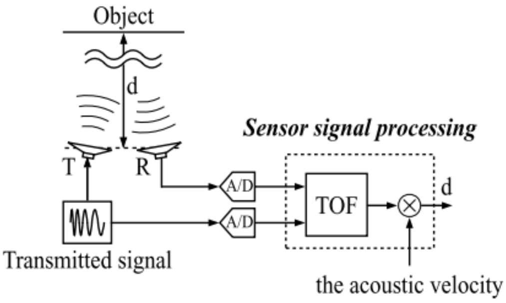

Figure 3.16: Pulse echo method [39]

The basic principle is same as in the case of photoelectric TOF sensors, the time of flight is measured and the distance is calculated using a known velocity of the pulse. To calculate TOF, typically pulse compression is utilized. It is a commonly used method in radar and communication technologies. In pulse compression the cross-correlation of the transmitted signal and it's echo is calculated. Best and unambiguous results are yielded when the signal is pseudo-random or frequency modulated, thus having high autocorrelation only with zero lag. Cross-correlation between reference signal $h(N-i)$ and the echo, $x(t-1)$ can be calculated with following formula:[39]

$$C(t) = \frac{1}{N} \sum_{i=0}^{N-i} h(N-1)x(t-i), \tag{3.18}$$

where N is the number of samples and t is time. The time of flight is the time in which the cross-correlation is maximized.[39]

Compared to photoelectric sensors, ultrasonic sensors offer better resistance to moisture and particles in the air. They are also not affected by external light sources. But unlike photoelectric sensors, they are affected by external acoustic noise. When noisy echoes and the reference signals are compared using cross-correlation, the maximum correlation value might get shifted by the noise.

Chapter 4

Implementation

4.1 Selection of a suitable sensor

To be able to choose a suitable sensor, the requirements should be cross-referenced. In this chapter the sensors introduced in the previous chapter are assessed by the requirements set in the introduction. The assessment is done on a sensor basis. First, the ability to resist environmental conditions, then aptitude of measuring the stress are assessed. Lastly, if sensors seem to be able to fulfil the measurement requirements the price is evaluated.

The strength of a vibrating wire sensor is that they have good resistance to environmental hazards. Hermetic sealing protects from moisture and corrosion. Protection form EMI is also possible depending on the material used in the sealing. Temperature dependence can be compensated. They are good for long term monitoring. Also, mounting of these sensors should be achievable with adhesive or screws. However the problems lie in the slow response times. The vibrating wire sensors are interrogated using different types of excitation signals, after which the sensor is let to rest until the output of the sensor becomes steady. This process of signal damping can last multiple minutes [13]. It makes measurement of a process that requires sampling frequency of at least 100 Hz impossible. Impact measurements have varying time spans, but they are not in the range of minutes, rather in milliseconds. For this reason vibrating wire technology can not be considered for impact measurements.

Like vibrating wire sensors, LVDTs offer robust sensor design, including shielding hermetic sealing. They are sealed and well protected. But unlike vibrating wires, LVDTs have no inherent weakness to fast dynamic changes. Accuracy, resolution, dynamic range, and particularly environmental resistance are all excellent, but the question is how is it possible to optimise the measurement system costs with these sensors. One LVDT sensor typically costs at minimum few hundred Euro. Also multiple sensors are needed for a single measurement point for to be able to measure principal strains. The foil strain gauges should be a cheaper option. For LVDTs' high expenses, they can be pruned out of the sensor considerations.

Four different accelerometer technologies were considered: piezoelectric, piezoresistive, capacitive and thermal. The environmental resistance of accelerometers depends highly on the possible encapsulation of the sensor. Luckily, since accelerometers have no additional mounting requirements other than tight fastening to the measured specimen, they can be fully covered with any protective method. They also have typically good shock resistance, some accelerometers can handle tens of thousands of g. Accelerometers' ability to estimate position depends even more on their accuracy than many other sensors, because the position must be integrated from the acceleration data. This is due to the error accumulating very fast with the noise. Based on merely sensors' resolution, bandwidth and noise floor it is still quite difficult to estimate how well accelerometers are able to measure impacts. However at least piezoresistive accelerometers can be pruned out, because they are only used for extremely high accelerations, thus not being optimal for this application. Accelerometers in general are very affordable meaning that the prospects of them being more cost effective than foil strain gauges are good. Accelerometers using piezoelement can be more expensive around 50–100 Euro per sensor, but the MEMS sensors are very affordable, around 5 Euro per sensor. However, the prices vary between sensor models and manufacturers. But the three types of accelerometers: capacitive, piezoelectric and thermal could be considered for testing.

SAW technology for sensor applications is still quite new, so their performance evaluation is difficult. Even though, these sensors are interrogated like vibrating wire sensors, SAW sensors can have high sampling rates. Interrogation can take few tens of nanoseconds, which means that very high sampling rates can be achieved. Prototypes of SAW sensors have been built that have sampling rates of 250 kHz [40]. SAW technology is based on RF waves and their signals can overlap in case of using multiple sensors at the same time. Though, it can be circumvented using various signal processing methods to identify the origins of each signal [41]. Cost assessment is can also be difficult, because of low commercial availability. SAW sensors show promise, but due to experimental nature of the sensor technology and scope of this thesis, SAW technology is not selected for further testing.

Semiconductor strain gauges are very similar to metallic foil gauges. Differences are that they have higher temperature dependence, higher sensitivity and low thermal expansion coefficient. The operating principle is quite same as well. Mounting of the sensor and the additional required hardware is naturally similar to their metallic counterparts, but the price of the sensor itself is a bit higher. Since the purpose of the thesis is to find a cheaper alternative it can be said that due to close similarity of the sensor properties and higher price, it is not reasonable to choose this sensor type.

Photoelectric sensors were originally strongly considered due to their good properties of long range measurement distance, simple mounting and no need for contact to the measurement point. The weakness of photoelectric sensors is related to their accuracy. The required accuracy of 0.2 mm is difficult to achieve with laser scanners. According to tests made on ten different high grade laser scanners by W. Boehler and A. Marbs, only one device achieved such a goal [42]. This sensor, Mensi S25 achieved it at range of 4 m, but the cost of such laser scanner is in thousands of Euro. With good grade laser scanner impact measurements should be feasible, but because of costs, laser scanners are not chosen for further testing.

Ultrasonic sensors are similar to the previously mentioned photoelectric sensors. Generally they have lower sampling rate, accuracy and range and are cheaper than their laser counterparts. Ultrasonic sensors being cheaper and mostly otherwise having inferior properties excluding for example immunity to error caused by external light sources they are not chosen for testing.

Below in table 4.1 is a rough estimation of characteristics of the compared sensors. The medium value given in the table is considered to be satisfactory.

	Sampling rate	Accuracy	Installation	Resilience	Price
Vibrating wire	low	high	medium	high	high
LVDT	high	high	medium	high	high
Accelerometer	high	medium	easy	medium	low
SAW	high	medium	difficult	medium	medium
Semicondct. SG.	high	medium	medium	medium	medium
Photoelectric	high	medium	medium	medium	high
Ultrasonic	low	low	medium	medium	low

Table 4.1: An estimation of sensor characteristics

4.2 Sensors

The next step was to choose sensors using the accelerometer technologies chosen in the previous section. Four sensors: Bosch Sensortec BMA456, MEMSIC MXR9150, Freescale Semiconductor FXLN8372Q and TE connectivity 805M1 were chosen for their suitable characteristics. The BMA456 and the FXLN8372Q are capacitive accelerometers. The MXR9150 is a thermal accelerometer and the 805M1 is a piezoelectric accelerometer. The major difference between the two capacitive accelerometers BMA456 and FXLN8372Q is that the BMA456 is a modern digital sensor containing microprocessor for added functionalities and the FXLN8372Q is a typical analogue sensor. The BMA456 can be interfaced with either SPI or I2C protocols. The analogue sensors output voltage messages. Each of the sensors have slightly higher acceleration range than the required 2 g acceleration range to ensure that testing is not bottlenecked by it. The MXR9150 has range of ±5 g, the 805M1 has ±20 g. Sensors BMA456 and the FXLN8372Q both have selectable acceleration ranges. The BMA456 can be set to ±2,4,6 or 8 g and FXLN8372Q can be set to either ±4 or 16 g. The ±3 dB bandwidths of the BMA456, MXR9150, FXLN8372Q and 805M1 are 8-684 Hz, 17 Hz, 2.7 kHz (X,Y axis) and 600 Hz (Z), 10 kHz accordingly. The bandwidth describes the frequency range the sensor can reliably measure. Note that the 801M1 is a single axis accelerometer, measuring only accelerations along Z-axis. [43][44][45][46]

Each of the sensors are relatively affordable, the thermal accelerometer MXR9150, capacitive accelerometers BMA456 and FXLN8372Q each costing approximately 5 Euro and the piezoelectric sensor 805M1 costing approximately 80 Euro. In case of not needing as much high-grade equipment like with strain gauges, the total cost of the system could be still lowered even if using a sensor as expensive as the 805M1. It was also confirmed that the sensors are not in the end of their lifespan to ensure that they are available now and in years to come for possible future projects.

4.3 Preliminary testing

The first logical task after the sensor selection was to do preliminary tests to see how accurate data they produce and whether it is even remotely possible to integrate position from the acceleration data. Calculating double integrals over a noisy signal is a difficult problem, as the noise is also integrated and therefore effect of noise is more detrimental for position estimates.

The preliminary test set-up consisted of a electronics prototyping board on which the sensors and a Teensy 3.6 microcontroller were mounted [47]. The sensors were continuously read with the microcontroller and the data was sent to a computer for signal processing. The prototyping board was moved and estimate trajectories were calculated using the measured accelerations. If at least the acceleration profiles would closely resemble the movement trajectories, then the tests would be considered as a pass. For curiosity's sake, the accelerations were also integrated to calculate position estimates to see how well such a simple method would work.

At the beginning, the program on the microcontroller checks the communication bus to BMA456 and configures few register values for it's operation. I2C connection to the sensors is checked by reading the CHIP_ID register value, which according to the manufacturer should return device identifier byte of 0x16. Then for to the sensor to start measuring, power save mode should be disabled by configuring the PWR_CTRL register. Then 500 microseconds should be waited before any further commands. This is for the register value to update. After this acceleration data acquisition should be enabled swapping the acc_en bit of the PWR_CTRL. After this the sensor was configured for 1600 Hz sampling, and for ±4 g measurements. It can be done by writing to configuration registers ACC_CONF and ACC_RANGE values of 0x8C and 0x01. The definitions of manipulated registers can be seen in the BMA456 datasheet.[43]

The acceleration data of BMA456 is in 6 bytes in the registers called DATA_0 – DATA_13, each axial acceleration consisting of two bytes. After the registers are read using I2C the values are stored in a 16 bit unsigned integer array. The data output of MXR9150, FXLN8372Q and 805M1 are analogue voltage signals and read by A/D conversion. After all the data have been read, it is being buffered and sent for data logging using serial communication with a baud rate of 9600 bits/second.

The data logging and signal processing was implemented by using Python 3.6 programming language, because it offers strong scientific calculation tools and signal processing libraries including NumPy and SciPy. And in case of needing high performance calculations it is still possible to wrap C/C++ code into it.

Data is being read for a set amount of time and stored to a timestamped text file. For it to be possible to analyse the data, it should first be preprocessed. The file is first parsed into a NumPy array. The first row is always removed as it most of the time contains an incomplete entry, because the data reading is not synchronized between the microcontroller and signal processing computer. Possible Nan values and incomplete data entries are also removed. The probability of a read error is very low, but since a dataset contains tens of thousands of rows, each containing multiple elements of different sensors, thus read errors are bound to happen. The data is also converted from voltage to acceleration format and also calibrated to be zero averaged when the sensors are in stationary state. Note that the thermal and capacitive accelerometers have offset of approximately 1 g on z-axis, because they can sense earth's static gravitational pull.

Originally, in the preliminary tests, after data preprocessing, the data was simply integrated twice to see how well the integrals behaved and whether the integrals could be used to calculate estimates for the position. The figures below (figures 4.1, 4.2, 4.3 and 4.4) contain the results that were the very first tests made with the chosen sensors. They are from a test in which the sensors are moved along all three axis. Though, only data of Z-axis is shown. The noise after initial movement is caused as a byproduct of the oscillations along X and Y-axis. Based on those results, it was decided that additional methods were needed for an improvement. First, with filtering the estimates accuracy could be possibly increased. Second, some method to remove drift of the position estimates was also needed.

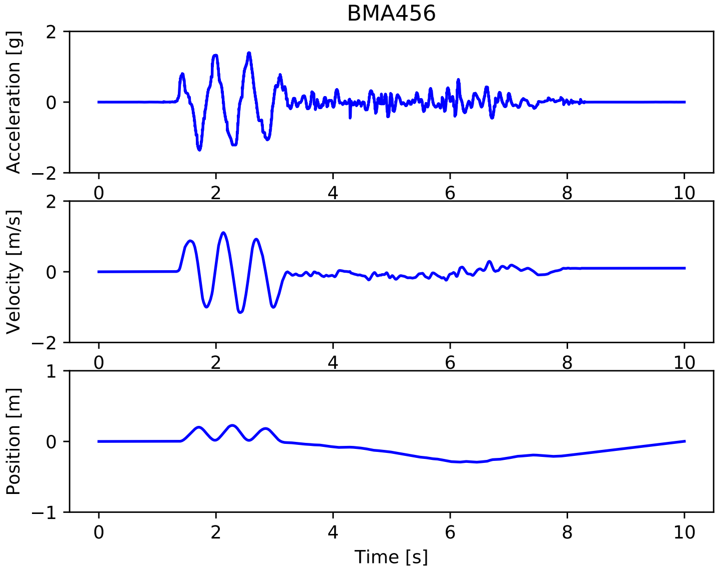

Figure 4.1: BMA456 position estimation

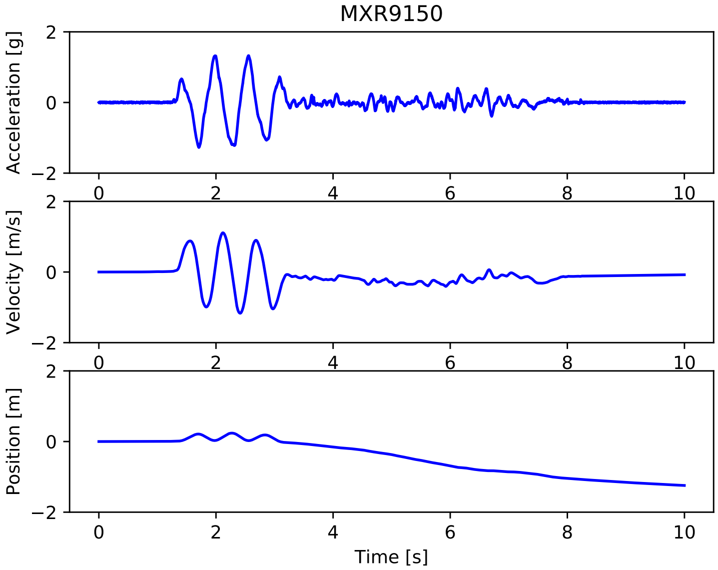

Figure 4.2: MXR9150 position estimation

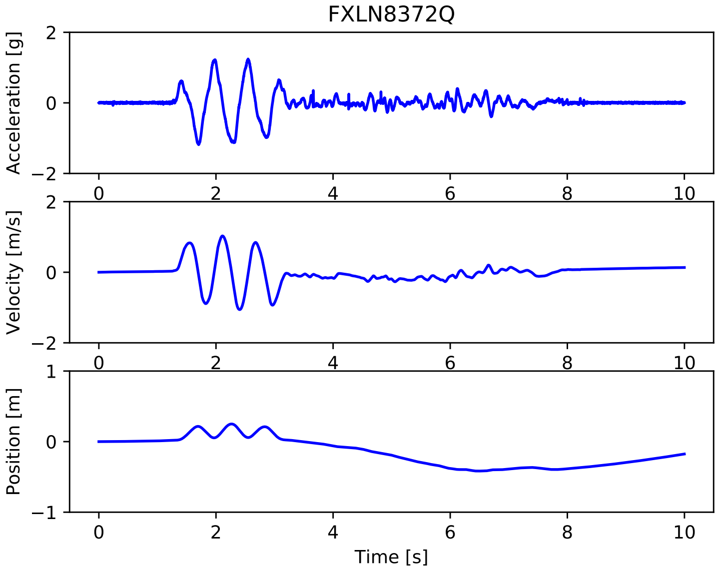

Figure 4.3: FXLN8372Q position estimation

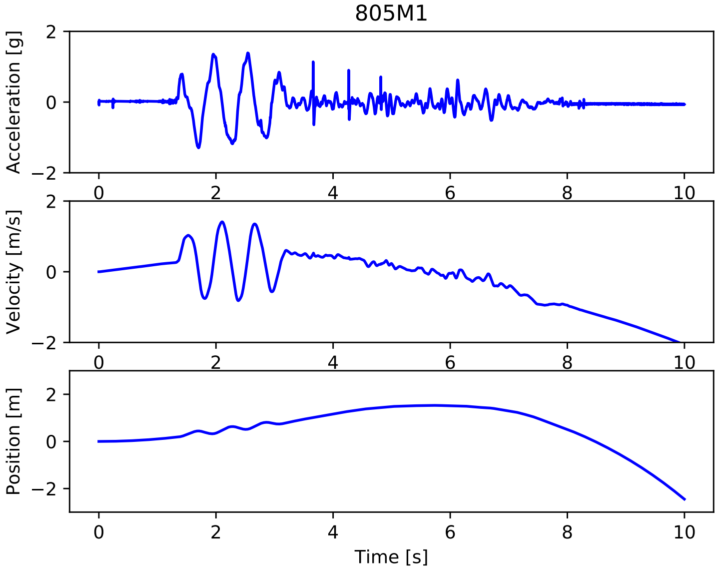

Figure 4.4: 805M1 position estimation

Results for preliminary testing, highly fluctuating estimates of velocity and position (figures 4.1 - 4.4) were not completely unexpected, because integrals in general are highly vulnerable to noise. And in these experiments two consecutive integrals are computed, which further increases the vulnerability to noise. Sources of noise and error are many, including inaccurate calibration, temperature dependence, limited bandwidth, external EMI. Even by reducing these sources of error, the used method is so prone to errors that the results would probably be similar.

If the results are compared, it can be seen that the FXLN8372Q and BMA456 have the least drift in position estimates. The estimates stay within ±1.0 m during the whole 10 s of continuous movement. The MXR9150 and 805M1 drift further than 1.5 m. These are not particularly good estimates for position, considering that in the tests the sensors were moved approximately in the range of ±0.3 m. However, this experiment did yield some valuable information: the estimates can not simply be calculated by integrating continuously.

4.4 Filtering

As previously mentioned, different filtering methods were experimented with. The first experimented method was the median filter. In the median filter each value in the signal is replaced with the median value of its neighbourhood. The size of the neighbourhood called the kernel affects the intensity of the smoothing. Properties of the median filter is that it preserves edges, but removes salt and pepper type of noise that consists of sparsely located high magnitude disturbances.

In addition to median filter, infinite impulse response (IIR) filtering was tested. With IIR filters certain unwanted noise frequencies can be filtered out. These IIR filters usually contain feedback and can be can be represented using following time domain equation [48]:

$$y(m) = \sum_{k=1}^{N} a_k y(m-k) + \sum_{k=1}^{N} b_k x(m-k), \tag{4.1}$$

where x is input, y is output of the filter. The Coefficients a_k and b_k are parameters defining the filter and can be derived from Laplace domain form of the filter. The simplest of the IIR filters is called the Butterworth filter. In the Butterworth filter the passband gain is maximally flat. The filter is defined by three parameters: zero frequency gain G_0, order N, and cut-off frequency ω_c. The filter's order affects the linearity of the region between passband and stopband. The cut-off frequency is the frequency after which the gain starts to decrease towards zero. The gain of a Butterworth filter of a squared signal is defined by the following transfer function in the frequency domain: [48]

$$G(j\omega) = |H(j\omega)|^2 = \frac{G_0}{1 + (\frac{\omega}{\omega_c})^{2N}} \tag{4.2}$$

Another common filter is the Chebyshew type-1 filter. Instead of optimizing the flatness of the passband like in case of the Butterworth filter, Chebyshew type-1 maximizes the rate of cut-off between passband and stopband by incorporating Chebyshew polynomials that induce ripple in the passband and some ringing in the stopband. The transfer function of Chebyshew type-1 filter is following: [48]

$$G(j\omega) = \frac{G_0}{1 + \epsilon^2 C_N^2(\frac{\omega}{\omega_\mathrm{c}})} \tag{4.3}$$

$$C_N(\frac{\omega}{\omega_\mathrm{c}}) = \cos(N\cos^{-1}(\frac{\omega}{\omega_\mathrm{c}})), |\omega| \leq \omega_\mathrm{c} \tag{4.4}$$

$$C_N(\frac{\omega}{\omega_c}) = \cosh(N\cosh^{-1}(\frac{\omega}{\omega_c})), |\omega| \geq \omega_c, \tag{4.5}$$

where C_N are Chebyshew polynomials (trigonometric representation) and ϵ is ripple coefficient. Chebyshew type-2, also known as the inverse Chebyshew filter is the counterpart to type-1. It also maximizes the rate of cut-off between passband and stopband, but instead of compromising the flatness of passband, Chebyshew type-2 adds ripple in the stopband. Chebyshew type-2 gain is defined by following transfer function: [48]

$$G(j\omega) = \frac{G_0}{1 + \frac{1}{\epsilon^2 C_N^2(\frac{\omega}{\omega_c})}} \tag{4.6}$$

Elliptic, or Cauer filter acts as a combination of the two Chebyshew filters. It maximizes the rate of cut-off between passband and stopband at the expense of adding ripple to both passband and stopband. The Elliptic filter is defined by: [48]

$$G(j\omega) = \frac{G_0}{1 + \epsilon^2 R_N^2(\gamma, \frac{\omega}{\omega_c})}, \tag{4.7}$$

where R_N is the Nth order elliptic rational function, γ is selectivity factor, ϵ is the ripple factor. The ripple factor affects the magnitude of ripple in the passband, while the selectivity and ripple factors both affect the ripple in the stopband. In the passband due to elliptic rational function gain has values between 1 and $1/\sqrt{1+\epsilon^2}$ and in the stopband the gain is between 0 and $1/\sqrt{1+\epsilon^2+R_N^2}$. [48]

The last experimented IIR filter was the Bessel filter. The Bessel filter has maximally flat phase delay, meaning that the different frequency components of the signal have as similar delay as possible after the filtering. Bessel filter gain is steady in the passband and decreases slowly after the passband until the frequency in multiple times higher than the cut-off frequency. This slow attenuation has a downside of not being able to filter noise frequencies close to the cut-off frequency. Bessel filter transfer function is defined by the Nth order Bessel polynomials B_N: [49]

$$H(j\omega) = \frac{G_0}{B_N(j\omega)} \tag{4.8}$$

$$B_N(s) = \sum_{k=0}^{N} s^k \frac{(2N-k)!}{2^{N-k} k!(N-k)!} \tag{4.9}$$

Gains and characteristics of the previously mentioned IIR filters can be seen in figure 4.5. Each of the filters in the figure are 5th order and their cut-off have been set to 150 Hz. The Chebyshew type 1 and Elliptic have ripple of 0.1 in passband. The ripple of the stopband for Chebyshew type 2 and Elliptic filters is also set to 0.1.

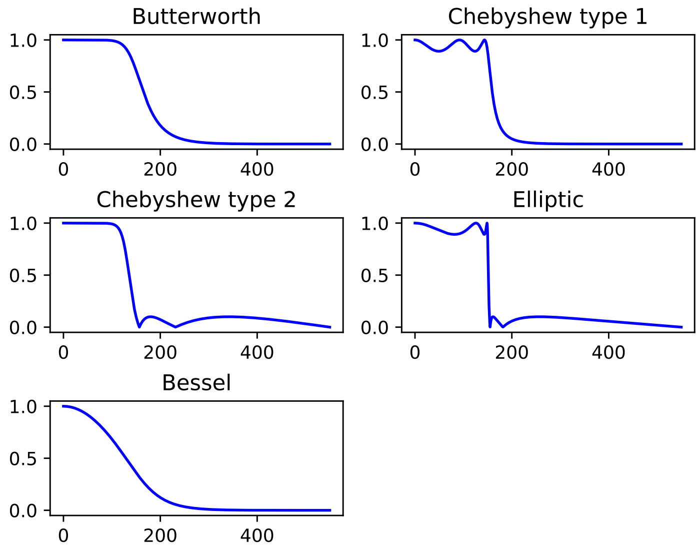

Figure 4.5: IIR filters

Next the tuning of the filters are discussed. The tests were done with a dataset containing nearly 800 impacts with varying force. First, the effects of different cut-off frequencies were tested with the simple Butterworth filter. The results can be seen in figure 4.6. It can be seen that the root-mean-square error (RMSE) decreases sharply for the three high band sensors until around 150 Hz. The RMSE settling down after 250 Hz indicates that the frequencies above that value do not contain any more relevant information for the position estimation. Thus, cut-off frequency should be set to approximately 200 Hz for the BMA456, the FXLN8372Q and for the 805M1. For the MXR9150 it should be set to around 60 Hz. The reason why the MXR9150 should have a lower cut-off frequency is that the sensor has so low bandwidth that most of the high frequency signals read by A/D conversion is only noise.

After choosing proper cut-off frequency, the aforementioned filters were tested for each sensor. The RMSE of the estimates with different filters can be seen in table 4.2. The ripple factors of The Chebyshew and Elliptic filters in this comparison were set to 0.1, because having very low ripple makes the filters identical to Butterworth filter, and increasing ripple excessively just

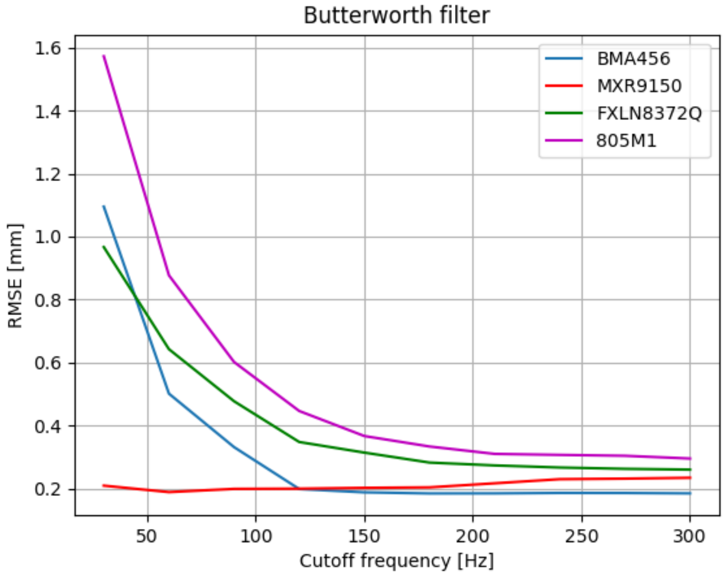

Figure 4.6: Effect of a lowpass filter

compromises the accuracy of the bands too much for position estimation. None of the filters improved the accuracy of BMA456 noticeably. Without and with any reasonable filter configuration error stays approximately the same. MXR9150 benefitted from filtering the most. Its RMSE without filtering is 0.30 mm and it can be lowered to 0.17 mm with the median filter. Kernel size of 5 gave the best result. Also the IIR filters performed well for MXR9150: they decreased RMSE by approximately 30% depending on the type and parameters of the IIR filter. FXLN8372Q has RMSE of 0.31 mm without any filtering and it only got higher with filtering. The 805M1 imroved its RMSE of 0.38 mm to 0.37 mm with any of the Chebyshew and Elliptic filters. The filtering results are is discussed and analysed more in depth in chapter 6.

In addition to low-pass filtering, the filters were also experimented in stop-band and high-pass filter configurations. The results of high-pass filtering were weak. Even if the threshold was set to a very low frequency (1-5 Hz), the estimate RMSE increased sharply. At 1 Hz, RMSE is approximately 0.3 mm and at 5 HZ it is approximately 0.7 mm. Increasing the cut-off frequency will further decrease the accuracy. The interpretation of this is that the measured impacts have low frequency components which are critical for the estimation. The explanation could be that the measurements were

	BMA456	MXR9150	FXLN8372Q	805M1
No filter	0.174	0.299	0.315	0.380
Median, kernel = 3	0.173	0.187	0.359	0.447
Median, kernel = 5	0.192	0.171	0.484	0.595
Butterworth	0.175	0.215	0.317	0.376
Chebyshew type-1	0.177	0.238	0.340	0.371
Chebyshew type-2	0.177	0.202	0.346	0.373
Elliptic	0.176	0.204	0.345	0.375
Bessel	0.174	0.179	0.355	0.405

Table 4.2: RMSE values of estimation with different filters

made by quite consistently hitting the accelerometers with approximately 1 Hz frequency. Such a peak of 1 Hz can be seen in the Fourier analysis as a high magnitude peak. Filtering this frequency affecting all the impacts, would create deformations on the acceleration profiles of the impacts, thus leading to high error.

To use stopband filtering the noise bands were sought from the Fourier analysis of the sensor's acceleration data (figures 4.7-4.10). The Fourier analysis gives the frequency domain representation of the data, which helps the observing of different frequency components. The idea was that bands containing smaller peaks, for example in figure 4.7 bands near 40 and 100 Hz, would contain noise. The other approach was to filter low magnitude areas between different frequency peaks. Filtering the smaller peaks decreased the estimation accuracy, thus these peaks contain information of the measured phenomenon. By filtering near the peaks, some success were found. In this particular 1 mm impact experiment for FXLN8372Q, a noise band was found at approximately 47 Hz, but the problem was mostly that the noise frequencies were on varying bands depending on experiment parameters, which made the bandstop filtering with a static band on a large batch of data suboptimal approach.

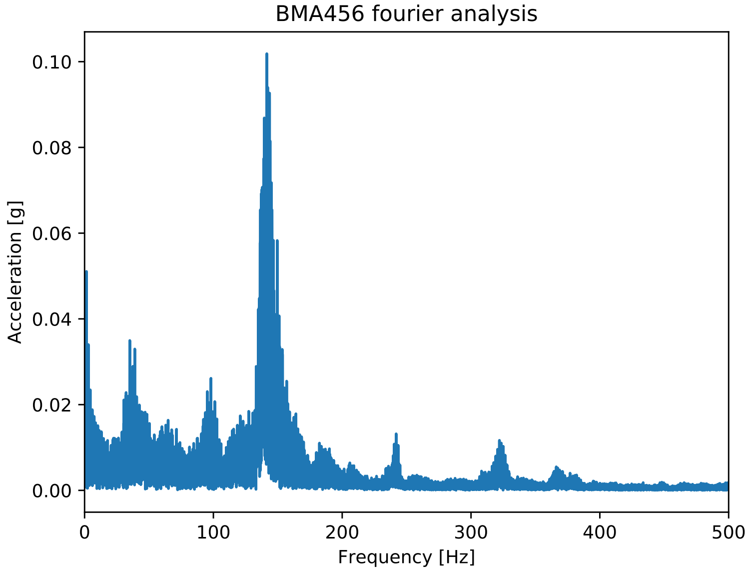

Figure 4.7: FFT transform of BMA456 1.0 mm impact measurement

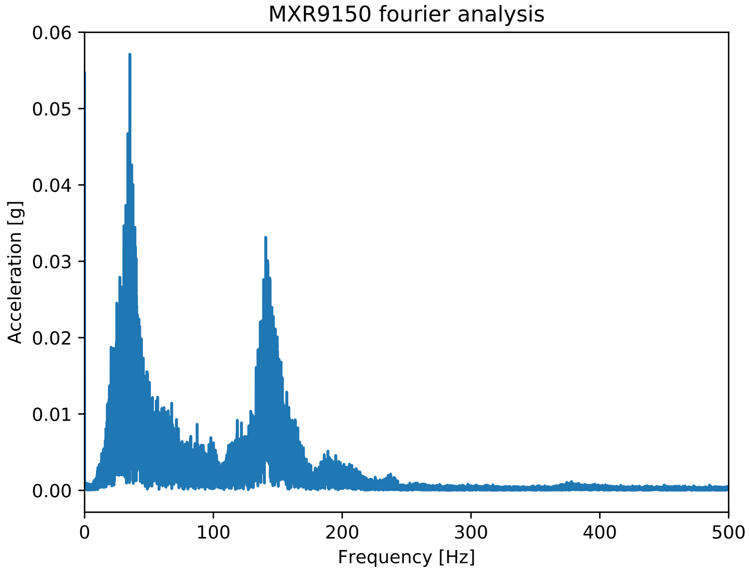

Figure 4.8: FFT transform of MXR9150 1.0 mm impact measurement

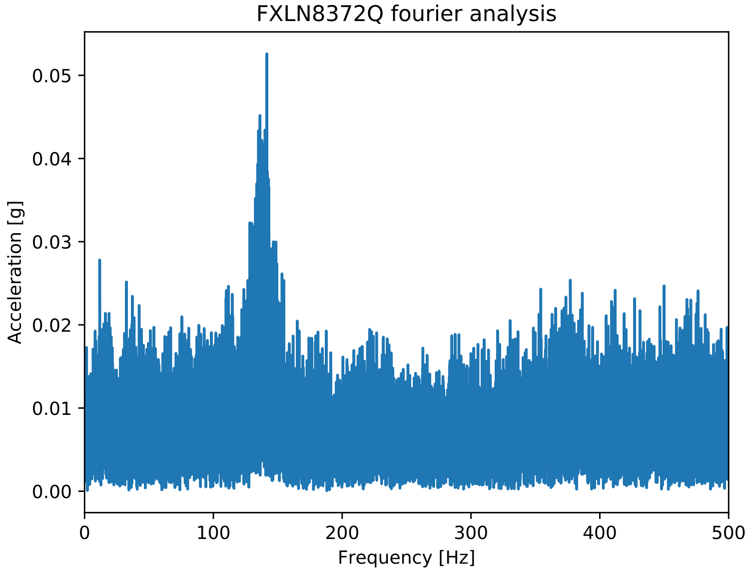

Figure 4.9: FFT transform of FXLN8372Q 1.0 mm impact measurement

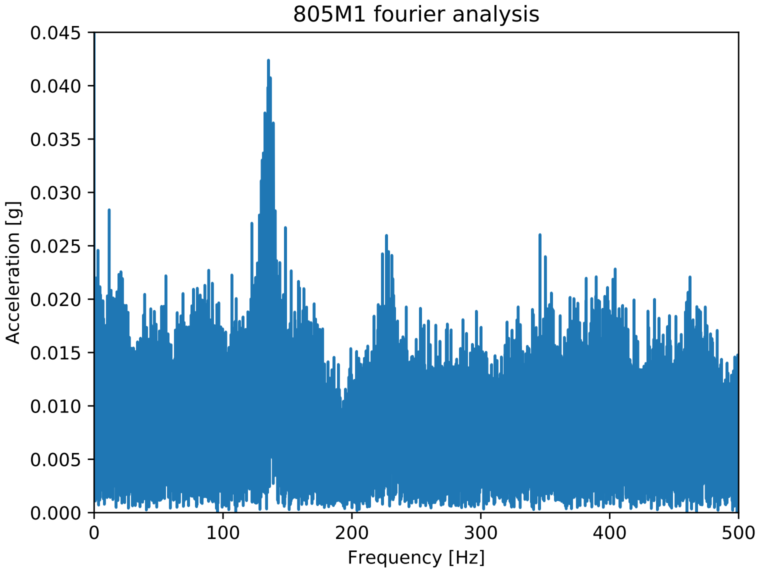

Figure 4.10: FFT transform of 801M1 1.0 mm impact measurement

4.5 Methods for reducing integral drift

One way to get rid of the integral drift is to reset the integrals before drift becomes a problem. Though, by resetting integrals the absolute position is lost. However, in this application movement information of a short timespan is enough to estimate impact loads. Initially, the integral reset was implemented by following method: first, detect peaks by comparing the values in a local neighbourhood. The amount of peaks would be restricted by setting a maximum peak density and a threshold for local maxima to be considered a peak. In case of density would be surpassed, the lowest peaks would be omitted. For each peak calculate starting and end index by comparing the signal to a threshold value near zero. Lastly, for each peak integrate twice from the start index to the end index. Sum the cumulative integrals to a zero signal.

This naive method (figure 4.11) did output reasonable results, though it did bear some weaknesses. First, it was realized that the velocity can naturally be still positive or negative when the acceleration reaches zero. Therefore instead of calculating integrals over one peak, it was decided that it is better to calculate it over the whole wave consisting of a negative and a positive peak (figure 4.12). This way the the movement during the deceleration is also included in the position estimate. It was also noticed that in case of measuring impacts the measurements consisted of multiple waves even though, some the vibration was filtered out of the signal by a low-pass filter. These vibrations would appear as position estimates for an impact, which is not necessarily harmful. But as it was wanted that the process of estimate reading and error assessment could automated, numerous position estimates caused by vibrations would increase average estimate error significantly.

In figures 4.11 and 4.12 are the two different methods of choosing integral span. On the upper sub-plot there are both the unfiltered (green) and 200 Hz Butterworth lowpass filtered signals (blue). Detected peaks are marked with red and blue. Integral span is marked with black. The lower sub-plot consists of all the position estimates of the data set and the average of the estimates.

For the previous reasons clustering was introduced. Clustering was used to combine measured and found peaks to impulse clusters. From these clusters only the first measured wave, the first negative and positive peaks were integrated. DBSCAN (Density based spatial clustering of application with noise) was chosen as the clustering method, because it finds clusters independently from shape, size and location of clusters to each other [50]. It also does not require a number of clusters to be set a priori. This is considered to

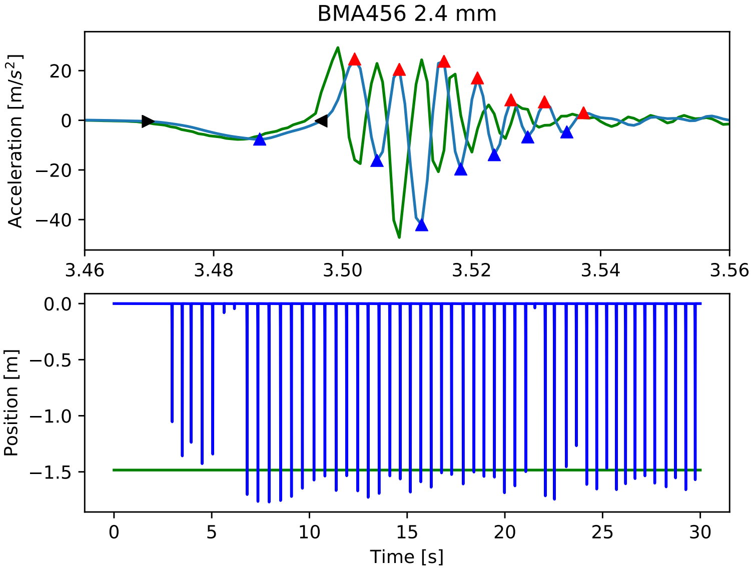

Figure 4.11: Integrating the first peak

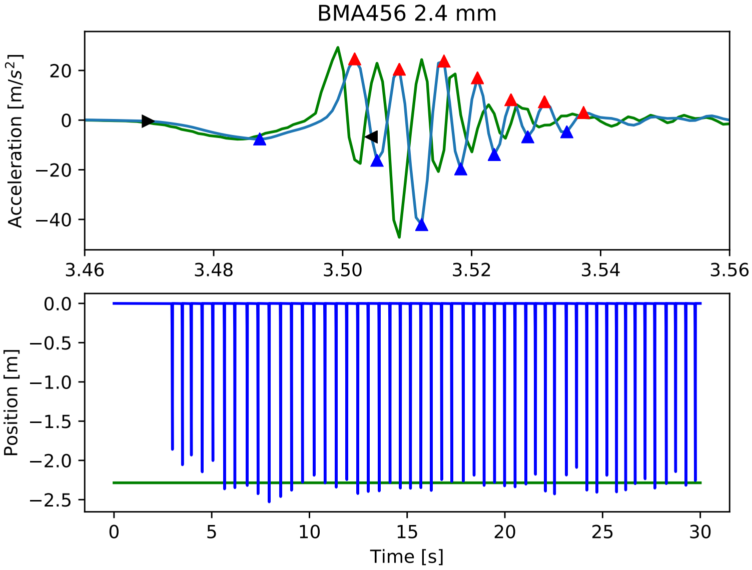

Figure 4.12: Integrating the first wave

be a strong benefit as the number of peaks and their distance vary between tests. It is very important to find the measured impacts even with different shapes and timings. DBSCAN depends on two parameters: a distance threshold parameter ϵ and a cluster minimum point parameter *MinPts*. Clusters are formed around core points. Core points are points that that have *MinPts* amount of points around it that are less than epsilon far away from it. Points that are not core points but are epsilon distance away from a core point belong to that cluster as well. Points that do not belong to a cluster are considered to be noise according to the algorithm. *MinPts* was chosen to be 1, because the smallest possible cluster would consist of two peaks. The number of samples between two points is considered to be the distance between the points. The ϵ threshold for it was set to 300, which translates to approximately to 0.27 s as the sampling frequency of the measurement system is 1100 Hz.

Another method experimented with, instead of clustering and finding specific integral indices by peak detection, was to high-pass filter the velocity and position data after the original low-pass filtered data was integrated once. The function of high-pass filtering was to remove small drift from the signal caused by initial integral, but still to preserve the higher frequency components caused by impulses. The idea is that only the frequencies above some threshold would contain the valuable information of the movement. The highpass filtering would also remove the drift from the estimates. The method worked with some success, if the sensors were accurately calibrated and cut-off frequencies chosen with care.

In figures 4.13 and 4.14 are the results of using lowpass filtering of 200 Hz for acceleration data and highpass filtering of 3 Hz for velocity and 1 Hz for position. The used data is from BMA456. Tests of 2 different experiments are shown. The upper sub-plot contains the velocity data. The unfiltered velocity is marked with blue and the filtered is marked with green. On the bottom sub-plot is the position estimation. The unfiltered position integrated from highpass filtered velocity is marked with green and the filtered position is marked with cyan. These figures show that with proper tuning the highpass filter method can estimate position reasonably well while also removing the drift from the data. The accuracy of this method was not par with using peak detection, clustering and integral resets. For this reason this highpass filtering was abandoned in favour of the previous method.

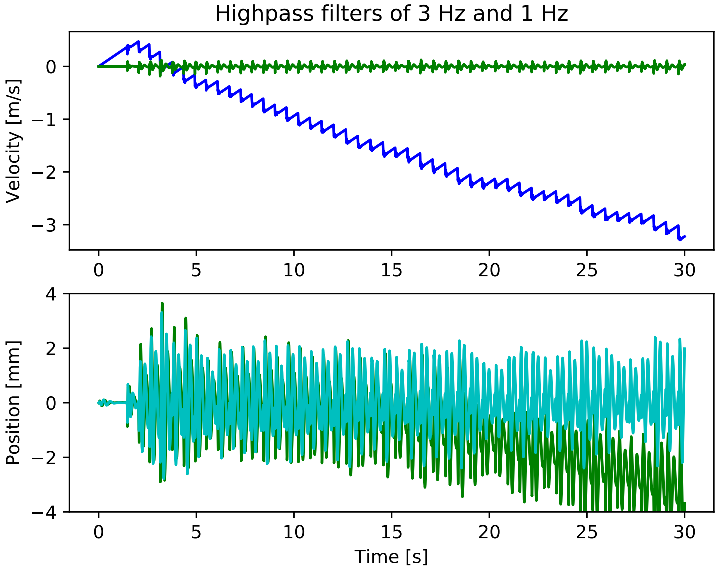

Figure 4.13: 2.0 mm impact estimation using 3 Hz and 1 Hz highpass filters

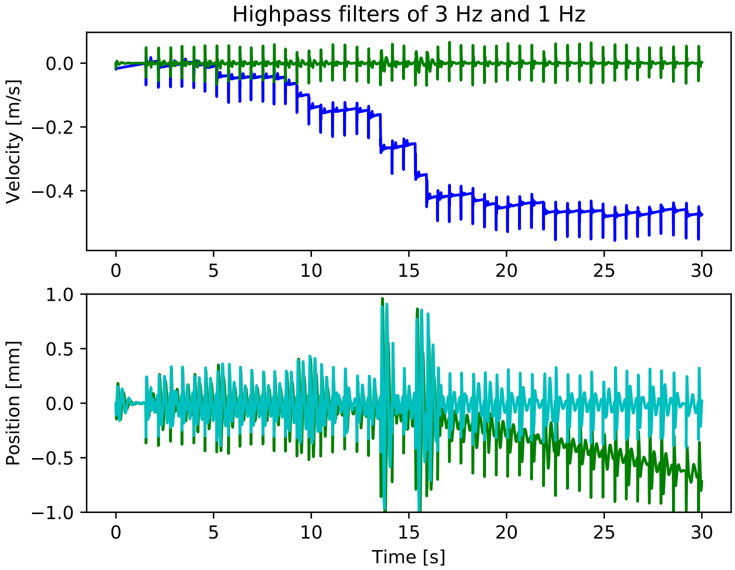

Figure 4.14: 0.5 mm impact estimation using 3 Hz and 1 Hz highpass filters

4.6 Measurement system

The purpose of the measurement system was to be able to verify the accuracy of the position estimates by limiting the movement of the sensors to a certain known distance. Then the estimates could be compared to the known position for a reference.

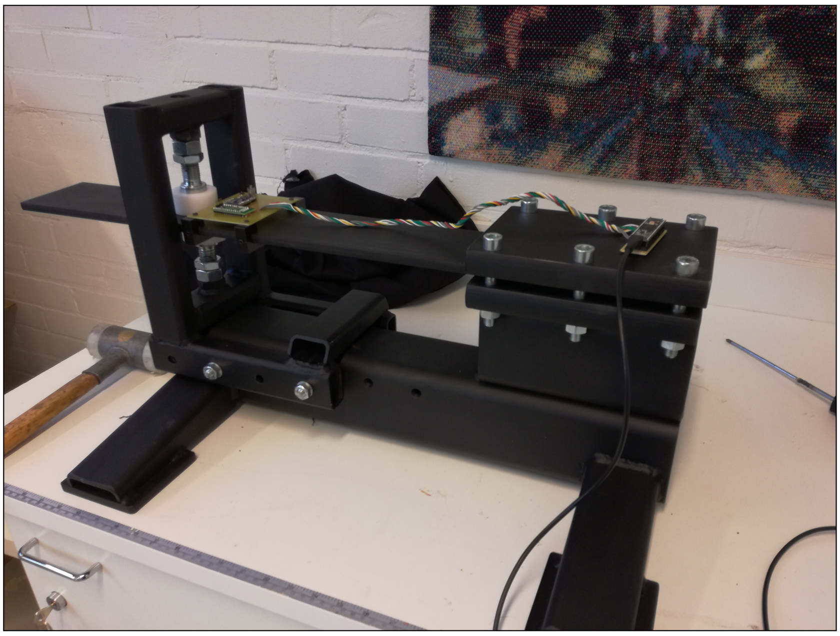

Figure 4.15: Measurement system

A design that fulfils the requirements for such previously mentioned system was to have a lever attached to a platform, figure 4.15. The sensors are mounted on the lever measuring its movement as it is being hit(Figure 4.17). The platform has also two stoppers to restrict the movement of the lever (Figure 4.16). One to constantly strain and push the lever down to ensure that the lever is always positioned the same place. The lower stopper is located underneath the lever, set to certain distance to limit the movement of it. When the lever would be hit, the sensors mounted on it would measure the acceleration profile of the movement as the lever moves the gap between the two stoppers.

The whole measurement system excluding the clamps for the circuit board was made of steel, thus it's weight keeps the system steady, decreasing noise from shaking test system. Also the legs of the platform have felt pads to decrease vibrations. Later in the testing it was noticed that the lever hitting

Figure 4.16: Measurement system stoppers

the hard plastic stoppers would induce strong noise to the acceleration data and for this reason also a pair of felt pads were attached to them.

In figure 4.17 the sensors can be seen to be mounted on the lever. Note that the circuit board design was made so that the actual sensor integrated circuits are on the same distance from the pivot point, minimizing the difference in the experienced acceleration. Also, the pull-up resistors of I2C bus can not be seen in the picture, as they are located under the BMA456 sensor module. In the later version of the test system, the I2C wires (grey) are shielded, because they induce strong EMI on the voltage signal lines. Note that the FXLN8372Q has high impedance outputs of approximately 10 kΩ. If the source impedance is high compared to the input impedance, the source impedance affects A/D conversion subsystem of the microcontroller by loss of bandwidth and response time, in addition to crosstalk between different A/D conversion channels. [51] Taking account that Teensy 3.6 with its on-board ARM Cortex-M4F microcontroller has input series resistance of 2 kΩ, the source impedance is too large [47]. For this reason a operational amplifier MCP6271 was put in series as voltage follower to reduce the impedance.

There are few presumptions regarding the test system. First, the bending of the lever is assumed to happen mostly in close vicinity of its fastening point. Otherwise the movement of the sensor and the gap between the stop-

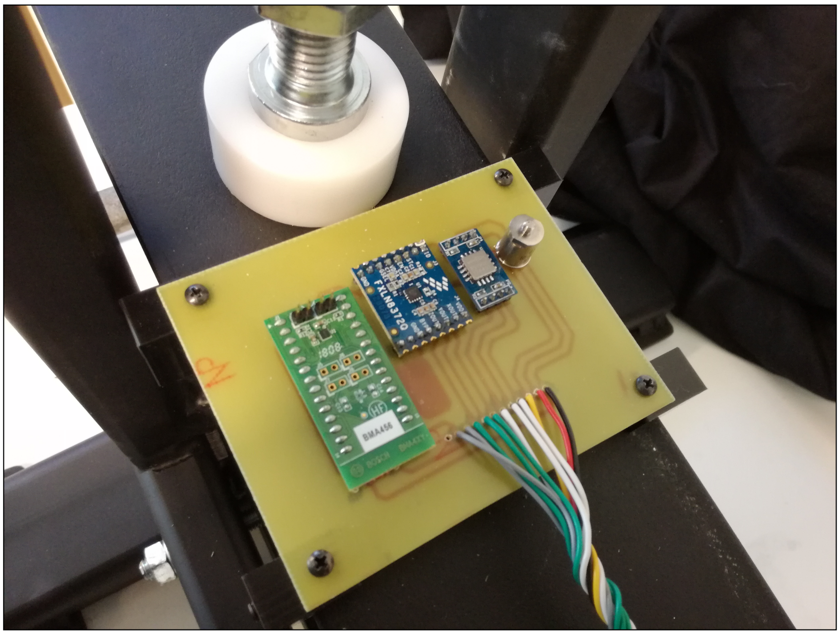

Figure 4.17: Sensors mounted on the measurement system

pers would not be comparable. In theory it is possible that there would form a standing wave on the lever that would disturb the measurements. Second, since the sensors are not exactly on top of the lever where it is stopped by the stoppers, the movement of the sensors is a bit lower than the set gap between the stoppers. The movement of the sensors is approximately 80% of the movement of the lever. This was both measured and verified by calculations. Though, the lesser movement is compensated by the felt pads that constrict approximately 0.3 mm. Therefore, in tests with low movements, the estimates will slightly overshoot and on higher values the estimates will undershoot.

Chapter 5

Results

This chapter contains results from the tests conducted with the measurement system.

The following figures are plots from five different experiments, each consisting of 40–50 impacts. All the sensors have plots from the same 0.5 mm, 1.0 mm, 1.5 mm, 2.0 mm and 2.4 mm experiments, therefore the results of each sensor are comparable and are within the required strain range. All of the following figures are in same format. The sub-plots on the left consist of a measured impact of the particular experiment. Black triangles describe the start and stop indices of the integral. Blue and red triangles mark the found peaks of the detected impact. The green signal is the unfiltered signal and blue signal is 200 Hz Butterworth low-pass filtered signal.

On the sub-plots on the right can be seen estimates for position marked with blue. They are the estimates calculated by integrating the range marked with black in the left sub-plot. The average of the estimate peak values is marked with green and standard deviation is marked with red.

The measurements have been made with varying impact forces. The experiments from 0.5 mm to 1.5 mm have been made by hitting the lever with a force high enough that it moves the lever to the lower stopper. The tests of 2.0 mm and 2.4 mm were made by pushing the lever to the stopper. Therefore, the latter have lower accelerations, but longer impact durations. Note that, the FXLN8372Q has an operational amplifier connected in voltage follower configuration, therefore there is similar phase delay in the signal compared to the 805M1. The signals of 805M1 are also delayed in all the measurements, but due to its integrated charge amplifier.

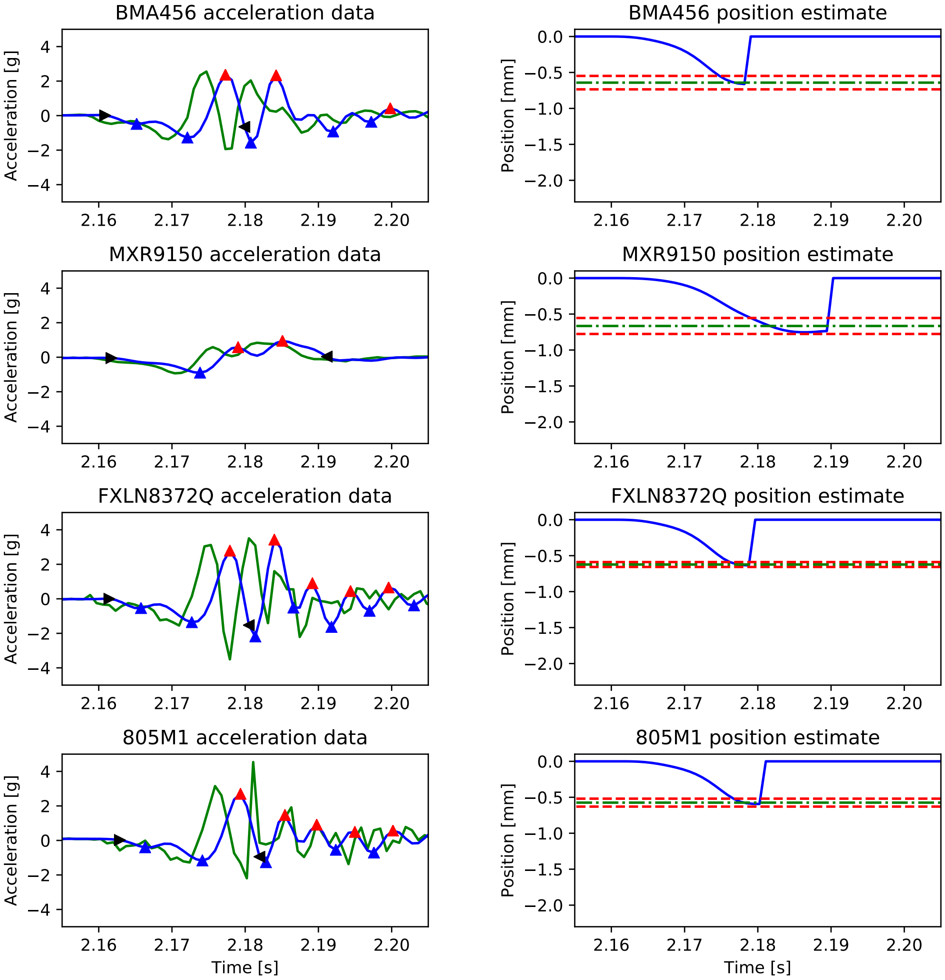

Figure 5.1: 0.5 mm impacts and position estimates

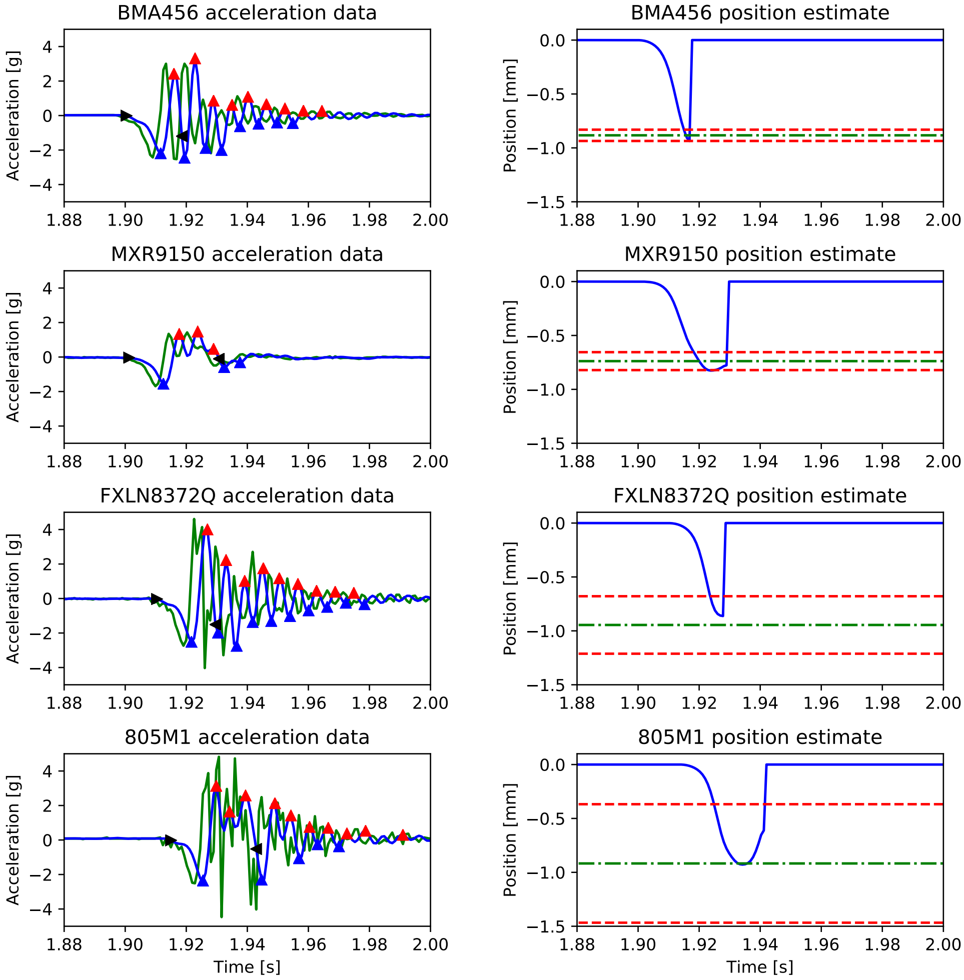

Figure 5.2: 1.0 mm impacts and position estimates

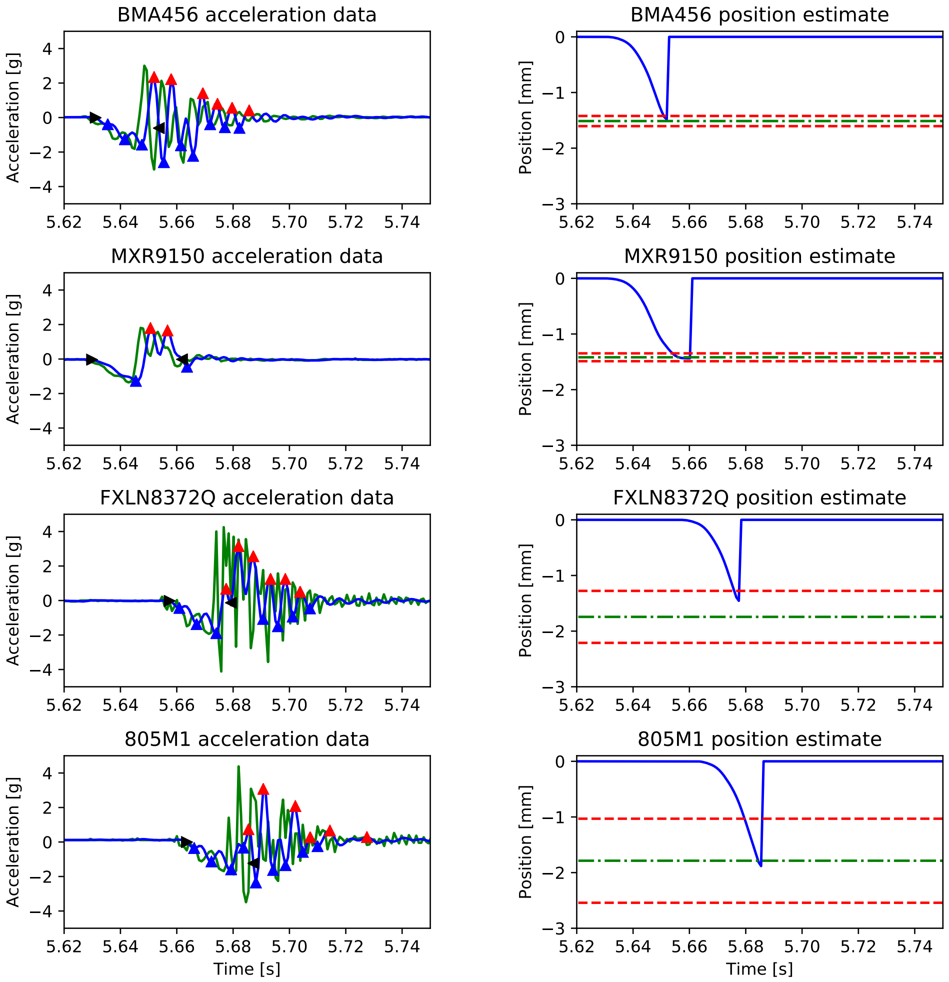

Figure 5.3: 1.5 mm impacts and position estimates

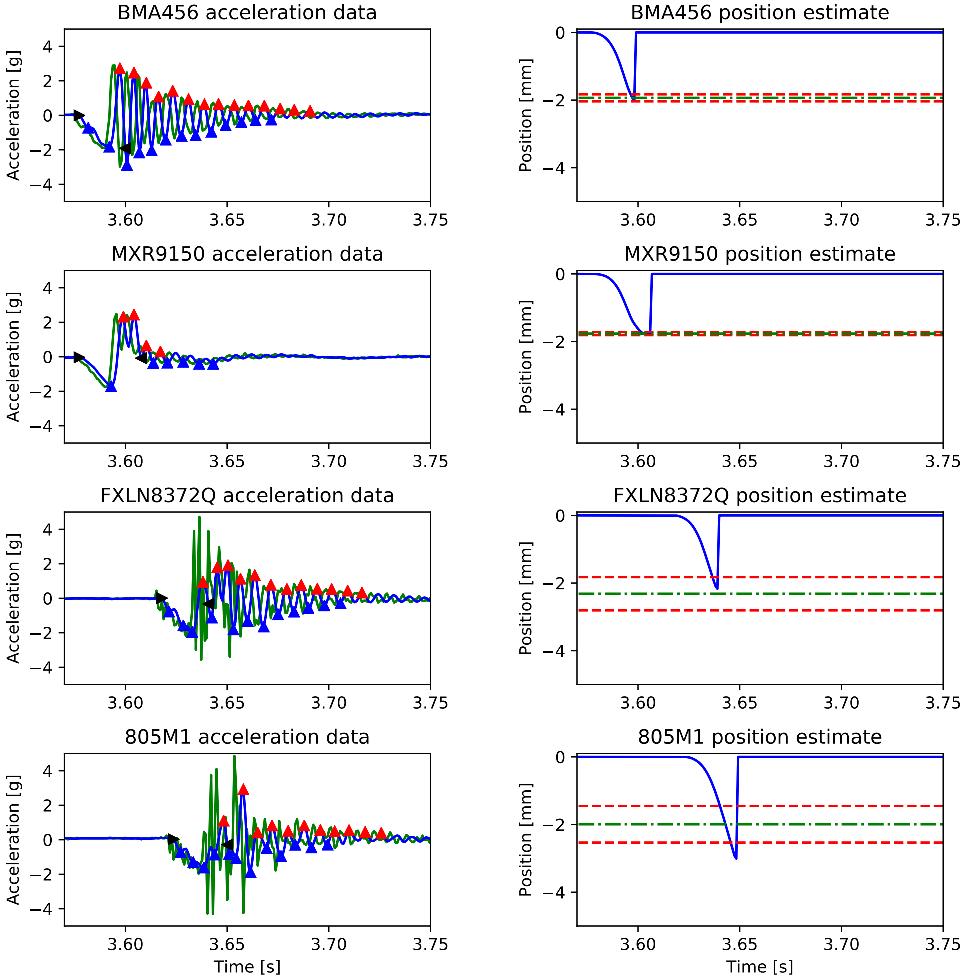

Figure 5.4: 2.0 mm impacts and position estimates

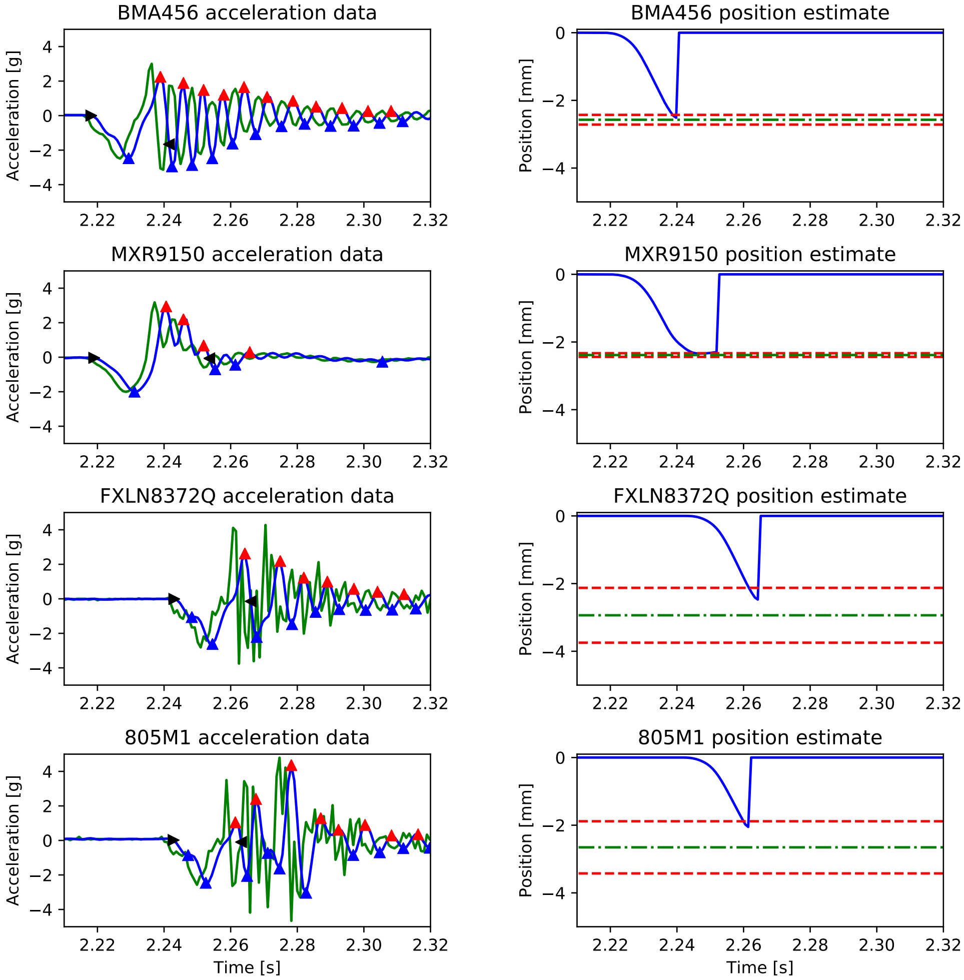

Figure 5.5: 2.4 mm impacts and position estimates

Chapter 6

Evaluation

When analysing the results (figures 5.1 – 5.5) of the measurement system with the improved estimation method of integral resets and clustering, we can see that the position estimates are no longer drifting and the estimates are noticeably consistent. Though, there is some constant error in the estimates for example in the 1.0 mm experiments (figures 5.2). The average is approximately 0.2 mm below the real value. The reason is most likely the fact that the impacts are made by hand and there was no method to ensure that the lever is always hit with high enough force to reach the lower stopper of the measurement system. Hitting the lever too hard would also create problems as the acceleration range of the sensors is limited and hitting too hard would cut the signal to the sensors maximum value. Sensors closing the maximum accelerations can be seen already in 1.5 mm tests (figure 5.3). As a note, the maximum value downwards of the sensor is practically reduced already by 1 g, because of earth's constant gravity.

On average the estimates are within 0.2 mm. Though, there is different amount of variance to each sensor's estimates. The MXR9150 has the smallest standard deviation of all the sensors, it is at its highest in the 1 mm experiment (figure 5.2) at 0.08 mm. The highest variance sensor is the 805M1 with standard deviation ranging from 0.1–0.5 mm. The BMA456 has variance similar to MXR9150, but slightly higher and FXLN8372Q has variance similar to 805M1, but slightly lower. Even though, MXR9150 having smaller variance than the BMA456, the estimates of the BMA456 on average are more accurate. This can easily be seen in figures 5.2 and 5.4. The reason why the sensors have varying estimation variance, is probably due to unequal levels of noise and makes estimation inconsistent. The difference in noisiness can be seen for example in the Fourier plots (figures 4.7–4.10). If the magnitudes of frequencies are evenly distributed, but the measured phenomenon is supposed to be repeating consistently, then there is noise in the measurements.

One source of constant error is the positioning of the sensors to the measurement system. The output of the system is always undershooting a bit due to sensors not being at the same distance as the stoppers. Though this is compensated by the felt pads that can be constricted up to 0.3 mm. In 0.5 mm tests (figure 5.1) the overshoot is maximized at approximately $0.8(0.5 + 0.3)$ mm $-$ 0.5 mm $=$ 0.14 mm. The undershoot of the estimation is at maximum: $0.8(2.4 + 0.3)$ mm $-$ 2.4 mm $= -0.24$ mm. This should especially be taken in considerations, when looking the average estimates in the figures 5.1 – 5.5.

Another thing to note is that the waveform of the outputs vary between the sensors. Especially the thermal accelerometer MXR9150 has considerably smoother signals than the others. This phenomenon can be explained by the bandwidth of the sensors. The manufacturer of MXR9150 promises bandwidth of only 17 Hz, compared to the other sensors having bandwidths of 600 Hz or higher. The effect of low bandwidth can be especially be seen in 1 mm tests. The capacitive and piezoelectric sensors can detect the oscillations after the initial shock, but the MXR9150 can barely notice it. In some cases this natural filtering can be an advantage as high frequencies are naturally filtered out. Though, generally if the dynamics of fast process is not well known, then the low bandwidth sensor is not probably the best option. Having low bandwidth leads to some valuable data being lost from the measured signal.

Some testing with filtering was also done. A good cut-off frequency for low-pass filtering was previously determined to be approximately 200 Hz. But based on comparing unfiltered and filtered signals' RMSE values given in table 4.2 we can see that the low-pass filtering unexpectedly did not have major improvements on the estimation accuracy for the capacitive and piezoelectric sensors. The three sensors BMA456, MXR9150 and 805M1 having broad bandwidth, leads to them being able to measure also high frequency noise components. Therefore, it's somewhat unexpected them to not improve estimation accuracy upon filtering frequencies higher than the measured phenomenon. It might be that the used method of clustering makes the filtering not that critical, as all signal peaks that are not the initial responses to a impact are omitted. Also, short and shielded wires decreases the noise induced to the communication bus that is probably one of the most vulnerable subsystem in respect to noise. As the system is well protected for its environment, the importance of low-pass filtering is lowered. In case of no or only minor noise filtering merely removes information out of the signal. The only sensor that seems to significantly improve it's estimation capabilities due to IIR filtering is the low bandwidth of 17 Hz sensor MXR9150. It's highest frequency components seems to be mostly noise.

One possible major reason why the estimation accuracy of the BMA456 does not improve is that it already has an internal lowpass filter set to 353 Hz. It is automatically set and depends only on the sensor's set sampling frequency. Though, it is set to a higher cut-off frequency than the filters used in this thesis. Possibly the manufacturer has already optimized the filtering for this sensors and for this reason, additional filtering is redundant if there is only minor noise in the communication bus.

The reason why the median filters fail with FXLN8372Q and 805M1, is probably the excess amount of noise of those sensors. The Median filters only function properly, when there is only sporadic impulse noise.

Even though MXR9150's bandwidth is rated to 17 Hz, it still is able to measure high frequency components to some degree, since in the Fourier analysis (figure 4.8) it can be seen that the oscillations of 150 Hz are being still measurable, but greatly dampened. Another observation is that BMA456 can clearly differentiate the amplitude of frequencies between 0 to 100 Hz. But MXR9150 seems to be mostly oblivious to any frequencies above 50 Hz, and FXLN8372Q coupled with 805M1 are not being able to measure the different frequencies in that range accurately. This can be also noticed from the figures 6.1–6.5 as the data of FXLN8372Q and 805M1 have noisier signals compared to those of MXR9150 and BMA456. Even if the gain of the sensor is within ±3 dB in certain band, it might not be flat, like in the case of FXLN8372Q and 805M1.

The types of filters tested were median filter, and four types of IIR filters: Butterworth, Chebyshew type-1, Chebyshew type-1, Elliptic and Bessel. The simple IIR filter, Butterworth filter alone filters the unwanted frequencies well. Though, the rate of cut off can be increased by switching to Chebychew or Elliptic filters. But the drawback is the added ripple. Chebyshew type-1 does not perform well if the ripple is even few decibels, because it compromises the passband. The passband should be flat as possible, because the frequencies of the passband are going to be integrated after the filtering. Any error caused by ripple affects the estimation. Setting the ripple close to zero gives similar results to Butterworth filter. Chebyshew type-2 filter performs generally better than Chebyshew type-1. Turns out that compromising the stopband is not as critical as flat passband. Though, trading flatness of stopband for higher rate of cut-off seems to decrease the estimation. Elliptic filter works well as it contains both of the characteristics of the Chebyshew filters. Though, ripple in the passband should still be set to a low value. Bessel filter's performance seemed a bit underwhelming for the BMA456, the FXLN8372Q and the 805M1 meaning that flatness of phase delay for those sensors has smaller impact to the filtering than the rate of cut-off frequency in application.

Overall, the best sensor seems to be BMA456: it has broad bandwidth and good accuracy. The drawbacks of that sensor are related to it's more complex configuration. It is very beneficial to be able to set the sensor settings such as sampling frequency, bandwidth, acceleration range to values needed, but there are some limitations related to the settings, for example bandwidth being tied to sampling rate, different axial measurements having different bandwidths even with the same settings and certain modes disabling some parameter values, such as higher sampling frequencies tied to high performance mode.

The low bandwidth sensor MXR9150 performs accurately in experiments of this thesis as well. Though, since the the sensor has low bandwidth restriction, it might be not be as good choice as the conditions of the actual environment might not be exactly the same as in the test system. Having such limitation might cause errors in measurements in which the dynamics are considerably faster. Though, this sensor has some benefits over the capacitive and piezoelectric MEMS sensors, as it is based on different technology. Thermal accelerometers do not have any moving structures inside of them and have natural cut-off frequency, thus they do not have DC offset due to resonance[52]. Measurements near natural frequencies can lead to resonance which could in the worst case break the sensor. This structure also makes the sensor more durable to physical trauma.

The sensor FXLN8372Q seems to be mostly outclassed by the BMA456. Even having wider bandwidth does not help if the band is not flat. At the very least it has option of increasing the acceleration measurement range from ±4 to ±16 g.

The piezoelectric sensor has some benefits over the previously mentioned sensors. It is constantly configured to ±20 g acceleration range measurements and still having high sensitivity. And in case the environment would rotate in relation to gravitational pull this sensor needs no recalibration as it is oblivious to static accelerations such as gravity. The other sensors need to be configured to know in which direction the gravity pulls, otherwise the 1 g of gravity would get integrated into the estimates and create huge errors. In the experiments this property did not see any use, but it might have major impact in practical applications.

Chapter 7

Conclusion

In this thesis the prospects of different sensor technologies for impact measurements have been researched and tested. Main goal was to implement impact measurement system for an already known structure. Metallic foil strain gauges and fibre Bragg grating sensors have been previously used, but for cost reasons cheaper alternative with similar accuracy is searched for. Since the structure is known the strain measurements can be also implemented with another method for example with position measurements.

For alternative implementation researched sensors include vibrating wire strain gauges, LVDTs, accelerometers, SAW sensors, semiconductor strain gauges, photoelectric sensors and ultrasonic sensors. It was concluded that accelerometers exhibit many good qualities especially for impact measurements in difficult conditions. Firstly, environmental resistance is good: they can be fully isolated from the environment and have high shock resistance. Secondly, the financial prospects of these sensors are also promising, as the sensors itself are cheap and do not need much additional equipment. Some installation costs can be also reduced due to easier mounting. For accelerometers, the mounting alignment angle matters less compared to strain gauges that requires it for accurate strain measurements. Smart accelerometer sensors with digital interfaces have good resistance against EMI, because high voltage bias is needed for a bit to change due to noise. And even the analogue sensors with voltage signals are strong contenders to strain gauges as the voltage signals are higher. Strain gauges' full scale output is in few mV, when the analogue accelerometers output voltage hundreds of times higher. Because of accelerometers' higher voltage signals induced voltage bias has to be also higher before it noticeably affects the estimation.

In the early stages of testing few methods were tried for position estimation. For continuous position estimation, it was experimented to highpass filter the velocity for removal of the drift caused by long integrals. The method showed some promise, but more accurate method seems to be to detect the impact peaks from the data and only to integrate over the measured peaks to shorten the integral timespan. Minimizing the integral timespan, also minimizes the drift. To detect maximums of the impacts, clustering in conjunction with peak detection was used. Using clustering to separate oscillations of different impacts and by integrating only the first oscillation of the cluster, gives the movement maximums caused by the impact. This gives a good representation of structure's strain.

To assess the accuracy of accelerometers' position estimates, some testing with a measurement system was also made. Tests were made with capacitive, thermal and piezoelectric accelerometers with varying test parameters to see how well each type of sensor performs in different scenarios. Both the impulse duration and sensor movement range were altered according to the known system's typical ranges. Based on the results it can be proven that accelerometers can be used for short term position change estimation with reliable accuracy. The RMSE was within the wanted tolerance 0.2 mm for the smart capacitive sensor BMA456 and for thermal accelerometer MXR9150. Though, the bandwidth of thermal accelerometers are typically very low, under 100 Hz, which makes them a risky choice for fast dynamic measurements, if the characteristics of the measured phenomenon is not well known.

The built test system design could still be improved. To further develop it, better method creating impacts should be developed to gain more control on how long the impulses take and hard is the impact. Also there should be some position sensor straight underneath the sensors instead of the stoppers to know the realized movement, so that the estimates would always have reliable reference value. Some impacts of a dataset were failed due to lever not doing the full range movement. Naturally, this can be easily circumvented by hitting lever harder, but then there is danger of exceeding the maximum accelerations of the sensor that they can measure, which would also ruin the data.

This project can be called a success, because the major goal of finding an alternative sensor with set requirements was found. It was proven that with current technology, accelerometers can be used for impact measurements to estimate the changes in position with relatively good accuracy. Depending on the dynamics of the impacts different accelerometer technologies excel. For small impacts as in this thesis capacitive and thermal accelerometer showed the most promise. But for higher accelerations piezoresistive and piezoelectric sensors are preferable.

Accelerometers have now been proven to be suitable for impact load estimation, which enables further development of the impact measurement system. The next step could be to verify the test results of this thesis with the actual system. The currently done tests are merely simulating the real measurement environment, thus tests in real environment should be done to reveal how well the simulations match with the actual system. Based on the tests done in real environment, changes should be done to the current software and hardware implementation. The software changes could include parameter tuning and changes to the algorithms used. The hardware should be changed to accommodate better to the new environment. The sensors should be insulated and hardware redundancy should be utilized for better fault tolerance. Furthermore, changing the microcontroller to a programmable logic controller should be considered for a better long term solution. Also, a human-machine interface (HMI) should be created to give operators and other crew the ability to receive feedback from the impact measurement system. HMI could be for example a set of meters to depict how close to the maximum load the system is by measurement location basis.

The results can also be used as a reference for accuracy and performance estimation for similar accelerometer projects. The more is known in the planning phase of a project, the more likely the original requirements are met. For this reason all the testing made in this thesis is useful information.

Bibliography

[1] B. Phelps and B. Morris. Review of hull structural monitoring systems for navy ships. `http://www.dtic.mil/dtic/tr/fulltext/u2/a588962.pdf`, 2013. Accessed: 2018-10-08.

[2] H. Lüke. The origins of the sampling theorem. *IEEE Communications Magazine*, 37(4):106–108, 1999. ISSN: 1558-1896.

[3] National Instruments. Strain gauge measurement - a tutorial. `http://elektron.pol.lublin.pl/elekp/ap_notes/NI_AN078_Strain_Gauge_Meas.pdf`, August 1998. Accessed: 2018-10-08.

[4] W. J. Eccles. *Pragmatic Electrical Engineering Systems and Instruments*. Morgan & Claypool, May 2011. ISBN: 9781608456727.

[5] Analog Devices. Strain gage measurement using an ac excitation. `https://www.analog.com/media/en/technical-documentation/application-notes/AN-683.pdf`, 2004. Accessed: 2018-10-31.

[6] M. Kreuzer. Strain measurement with fiber bragg grating sensors. `http://www-personal.umich.edu/~bkerkez/courses/cee575/Handouts/7FBGS_StrainMeasurement_mo.pdf`, 2006. Accessed: 2018-10-08.

[7] D. Seo, D. Yoon, I. Kwon, and S. Lee. Sensitivity enhancement of fiber optic fbg sensor for acoustic emission. In *Nondestructive Characterization for Composite Materials, Aerospace Engineering, Civil Infrastructure, and Homeland Security 2009*, volume 7294, page 7. International Society for Optics and Photonics, 2009. DOI: 10.1117/12.821516.

[8] Smartscan sbi. `https://www.smartfibres.com/products/smartscan-sbi`. Accessed: 2018-09-13.

[9] National Instruments. Fundamentals of fiber bragg grating (fbg) optical sensing. `http://www.ni.com/white-paper/11821/en/`, 1 2016. Accessed: 2018-10-08.

[10] R. Maaskant, T. Alavie, R. M. Measures, G. Tadros, S. H. Rizkalla, and A. Guha-Thakurta. Fiber-optic bragg grating sensors for bridge monitoring. *Cement and Concrete Composites*, 19(1):21–33, 1997. DOI: 10.1016/S0958-9465(96)00040-6.

[11] J. M. Gere. *Mechanics of Materials.* B. Stenquist, Belmont, California, USA, 6 edition, 2004. ISBN: 0-534-41793-0.

[12] L. Peel. Strain transformation and rosette gage theory. `http://users.tamuk.edu/kfldp00/MEIE_Peel_website/Courses/Meen5330/strain-gage-rosette-theory_GA_Tech.pdf`. Accessed: 2018-10-08.

[13] P. V. Guerrero, H. K. M. Vicente, and A. de Gortari. Comparison of excitement methods of vibrant wire sensors. *African Journal of Physics ISSN*, 3(4):78–80, 2016. ISSN: 9821-5213.

[14] Vibrating wire arc weldable strain gauge. `http://www.avantech.in/products/vibrating-wire-arc-weldable-strain-gauge.aspx`. Accessed: 2018-09-13.

[15] P. Choquet, F. Juneau, P. J. Debreuille, and J. Bessette. Reliability, long-term stability and gage performance of vibrating wire sensors with reference to case histories. In *Proceedings of the 5th International Symposium on Field Measurements in Geomechanics*, volume 1, page 3, 1999.

[16] P. Sreeshylam, P. Ravisankar, K. Parivallal, S. Kesavan, and S. Sridhar. Condition monitoring of prestressed concerete structures using vibrating wire sensors. *International Journal of COMADEM*, 11(3):46, 2008. ISSN: 1363-7681.

[17] H. Zumbahlen, editor. *Basic linear design.* Analog Devices, Inc., 2007. ISBN: 0-916550-28-1.

[18] M. Martino, A. Danisi, R. Losito, A. Masi, and G. Spiezia. Design of a linear variable differential transformer with high rejection. *IEEE Transactions on Magnetics*, 46(2):674–677, 2010. ISSN: 1941-0069.

[19] L. Hudson. Temperature considerations when specifying lvdt linear position sensors. `https://www.techbriefs.com/component/content/`

`article/tb/techbriefs/mechanics-and-machinery/18750`, 2013. Accessed: 2018-10-08.

[20] TE connectivity. Choosing the right type of accelerometer. `https://www.mouser.com/pdfdocs/choosing-the-right-accelerometer-white-paper.pdf`, 2017. Accessed: 2018-10-08.

[21] J. Fennelly, S. Ding, J. Newton, and Y. Zhao. Thermal mems accelerometers fit many applications. *Sensor Mag*, 3:18–20, 2012.

[22] V. Sharapov. *Piezoceramic Sensors*. Springer-Verlag, Berlin Heifelberg, 1 edition, 2011. ISBN: 978-3-642-15311-2.

[23] J. Shiroshi and I. Chopra. Fundamental understanding of piezoelectric strain sensors. *Journal of intelligent material systems and structures*, 11(4):246–257, 2000. DOI: 10.1106/8BFB-GC8P-XQ47-YCQ0.

[24] J. Karki. Signal conditioning piezoelectric sensors. `http://www.ti.com/lit/an/sloa033a/sloa033a.pdf`, September 2000. Accessed: 2018-10-08.

[25] M. Andrejašic. Mems accelerometers. `http://faculty.uml.edu/xwang/16.541/2010/MEMS_accelerometers.pdf`, 2008. Accessed: 2018-10-08.

[26] Meggit. Steps to selecting the right accelerometer. `https://endevco.com/news/newsletters/2012_07/tp327.pdf`, 2012. Accessed: 2018-10-08.

[27] T. K. Bhattacharyya and A. L. Roy. *MEMS Piezoresistive Accelerometers*. Springer, India, 2014. DOI:10.1007/978-81-322-1913-2_2.

[28] A. Albarbar, S. Mekid, A. Starr, and R. Pietruszkiewicz. Suitability of mems accelerometers for condition monitoring: An experimental study. *Sensors*, 8(2):784–799, 2008. DOI: 10.3390/s8020784.

[29] M. Rahul, B. Joydeep, M. Pradip, and G. Kumar. A review of micromachined thermal accelerometers. *Journal of Micromechanics and Microengineering*, 27(12):123002, 2017. DOI: 10.1088/1361-6439/aa964d.

[30] R. Stoney. Characterisation of a wireless passive surface acoustic wave strain sensor. `https://pdfs.semanticscholar.org/0953/2590695c8058189257d847cee5a6b5146439.pdf`, 2013. Accessed: 2018-10-08.

[31] Global strain gage based sensor market 2018 by competition landscape. `http://www.energyindexwatch.com/tag/global-strain-gage-based-sensor-market-region`. Accessed: 2018-09-13.

[32] Kulite semiconductor products INC. Strain gauge manual. `https://www.kulite.com/docs/products_overview/StrainGageManualDigital.pdf`. Accessed: 2018-10-08.

[33] M. A. Hopcroft. What is the young's modulus of silicon? *JOURNAL OF MICROELECTROMECHANICAL SYSTEMS*, 19(2):229–238, 2010. ISSN: 1941-0158.

[34] S. Yang and N. Lu. Gauge factor and stretchability of silicon-on-polymer strain gauges. *Sensors*, 13(7):8577–8594, 2013. DOI: 10.3390/s130708577.

[35] T. Frank, M. Khatri, M. Fiedler, A. Gruen, M. Kermann, A Cyriax, and T. Ortlepp. Miniaturized silicon strain gauge elements to accurately measure mechanical quantities. pages 61–65, AMA Conferences 2015, Nürnberg, Germany, 2015. Proceedings SENSOR 2015. ISBN: 978-3-9813484-8-4.

[36] K. Konolige, J. Augenbraun, N. Donaldson, C. Fiebig, , and P. Shah. A low-cost laser distance sensor. In *Robotics and Automation*, pages 3002–3008. IEEE, 2008. ISBN: 978-1-4244-1646-2.

[37] C. Bamji S. B. Gokturk, H. Yalcin. A time-of-flight depth sensor system description, issues and solutions. In *Computer Vision and Pattern Recognition Workshop*, pages 35–35. IEEE, 2004. DOI: 10.1109/CVPR.2004.291.

[38] IFM electronic. Training manual photoelectric sensors. `http://www.ifm.com/obj/s200e.pdf`, 2003. Accessed: 2018-09-13.

[39] S. Hirata, M. K. Kurosawa, and T. Katagiri. Cross-correlation by single-bit signal processing for ultrasonic distance measurement. *IEICE Transactions on Fundamentals of Electronics, Communications and Computer Sciences*, 91(4):1031–1037, 2008. ISSN: 1745-1337.

[40] F. Lurz, T. Ostertag, B. Scheiner, R. Weigel, and A. Koelpin. Reader architectures for wireless surface acoustic wave sensors. *Sensors*, 18(6):1734, 2018. DOI: 10.3390/s18061734.

[41] J. Humphries, M. Gallagher, and D. Malocha. Analysis of inter-sensor interference for wireless saw sensors. In *Ultrasonics Symposium (IUS), 2014 IEEE International*, pages 396–399. IEEE, 2014. ISSN: 1051-0117.

[42] W. Boehler and A. Marbs. Investigating laser scanner accuracy. *The International Archives of Photogrammetry, Remote Sensing and Spatial Information Sciences*, 34(Part 5):696–701, 2003.

[43] Bosch Sensortec. Bma456 digital, triaxial acceleration sensor. `https://ae-bst.resource.bosch.com/media/_tech/media/datasheets/BST-BMA456-DS000-01.pdf`, 2017. Accessed: 2018-09-13.

[44] Memsic. Low cost 5 g tri axis accelerometer with ratiometric outputs mxr9150gm. `https://www.memsic.com/userfiles/files/Datasheets/Accelerometer-Datasheets/MXR9150GM__Rev_D.pdf`, 2007. Accessed: 2018-09-13.

[45] Freescale Semiconductor Inc. Xtrinsic fxln83xxq 3-axis lowpower analog-output accelerometer. `http://cache.freescale.com/files/sensors/doc/data_sheet/FXLN83xxQ.pdf`, 2004. Accessed: 2018-09-13.

[46] TE connectivity. Model 805m1 accelerometer. `https://www.te.com/commerce/DocumentDelivery/DDEController?Action=showdoc&DocId=Data+Sheet%7F805M1_Accelerometer%7FA2%7Fpdf%7FEnglish%7FENG_DS_805M1_Accelerometer_A2.pdf%7F805M1-0020`, 2018. Accessed: 2018-09-13.

[47] NXP Semiconductors. Kinetis k66 sub-family 180 mhz arm cortex-m4f microcontroller. `https://www.nxp.com/docs/en/data-sheet/K66P144M180SF5V2.pdf`, 2017. Accessed: 2018-09-13.

[48] P. Podder, M. Hasan, R. Islam, and M. Sayeed. Design and implementation of butterworth, chebyshev-i and elliptic filter for speech signal analysis. *International Journal of Computer Applications*, 98(7), 2014. DOI: 10.5120/17195-7390.

[49] S. Winder. *Analog and Digital Filter Design.* Newnes, 2 edition, 2001. ISBN: 0-7506-7547-0.

[50] M. Verma, M. Srivastava, N. Chack, A. Diswar, and N. Gupta. A comparative study of various clustering algorithms in data mining. *International Journal of Engineering Research and Applications (IJERA)*, 2(3):1379–1384, 2012. ISSN: 2248-9622.

[51] J. Childers. Adc source impedance. `http://www.ti.com/lit/an/spna088/spna088.pdf`, 2004. Accessed: 2018-09-13.

[52] J. Fennally. Capacitive vs thermal mems for high-vibration applications. `https://www.automation.com/automation-news/article/capacitive-vs-thermal-mems-for-high-vibration-applications`, 2016. Accessed: 2018-10-08.